Journal Pre-proofs

Fractographical quantitative analysis of EN-AW 2024 aluminum alloy after creep pre-strain and LCF loading

W. Macek, A. Tomczyk, R. Branco, M. Dobrzyński, A. Seweryn

Please cite this article as: Macek, W., Tomczyk, A., Branco, R., Dobrzyński, M., Seweryn, A., Fractographical quantitative analysis of EN-AW 2024 aluminum alloy after creep pre-strain and LCF loading, *Engineering Fracture Mechanics* (2023), doi: https://doi.org/10.1016/j.engfracmech.2023.109182

This is a PDF file of an article that has undergone enhancements after acceptance, such as the addition of a cover page and metadata, and formatting for readability, but it is not yet the definitive version of record. This version will undergo additional copyediting, typesetting and review before it is published in its final form, but we are providing this version to give early visibility of the article. Please note that, during the production process, errors may be discovered which could affect the content, and all legal disclaimers that apply to the journal pertain.
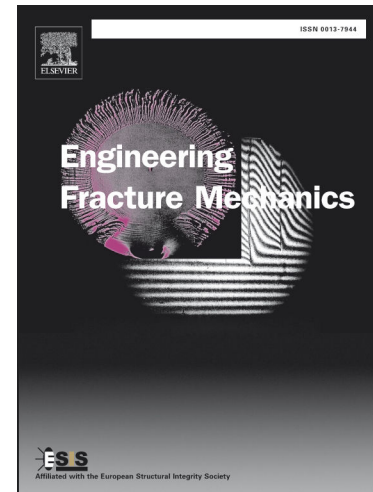
Fractographical quantitative analysis of EN-AW 2024 aluminum alloy after creep pre-strain and LCF loading

W. Macek[a], A. Tomczyk[b]✉, R. Branco[c], M. Dobrzyński[a], A. Seweryn[a]

[a]   Gdańsk University of Technology, Faculty of Mechanical Engineering and Ship Technology, Gdańsk, Poland

[b]   Białystok University of Technology, Faculty of Mechanical Engineering, Wiejska 45C Str, 15-351 Białystok, Poland, a.tomczyk@pb.edu.pl

[c]   University of Coimbra, CEMMPRE, Department of Mechanical Engineering, Coimbra, Portugal

Highlights

- The effect of creep pre-strain on LCF failure is examined via fractographic analysis for 2024 AA
- S_x, V_x and D_f fracture surface parameters were strongly dependent on the creep pre-strain history
- A new damage parameter P combining fracture surface topography and load features is introduced
- The proposed damage parameter P can successfully estimate the fatigue lifetime for 2024 AA

Abstract:

This paper explores the applicability of a new damage parameter combining both fracture surface topography and loading features to estimate the fatigue lifetime under creep pre-strain and low-cycle fatigue loading. Fractures of EN-AW 2024 aluminum alloy caused by mixed creep and low-cycle fatigue loading are experimentally characterized and quantified via surface topography analysis. The specimens were preliminary damaged in a creep process at elevated temperature (100°C, 200°C, or 300°C) considering two strain levels for each temperature. The specimens with preliminary damage were then subjected to fatigue tests at room temperature. The post-failure fracture surfaces were examined with an optical profilometer, and the focus was placed on the relationship between the creep-fatigue damage and the associated fracture surface topography parameters. In addition, an original fatigue life prediction model based on both the surface topography values and the applied strains was proposed and verified. The proposed model can be helpful for post-mortem analysis of engineering components subjected to fatigue loading accounting for creep pre-strain.

Keywords:

Creep; fatigue life; low-cycle fatigue; pre-strain effect; fracture surface topography; fractal dimension.

Nomenclature:

a, b, c, d	-	exponential coefficients
A_ω, n_ω	-	material parameters
b_1, c_1	-	fatigue strength and ductility exponents
D_f	-	fractal dimension
E	GPa	Young's modulus
mr	-	material ratio
f	Hz	frequency of cyclic loads
N_f	cycles	number of cycles to failure
P		topographic stress factor
R^2	-	coefficient of determination
R_ε	-	strain ratio
Sa	mm	arithmetical mean height
Sk	mm	core height
$Smrk1$	%	upper bearing area
$Smrk2$	%	lower bearing area
Sq	mm	root mean square height
Sp	mm	maximum peak height
Spk	mm	reduced peak height
Ssk	-	skewness
Sv	mm	maximum pit depth
Svk	mm	reduced pit depth
Sx		height parameters
Sz	mm	maximum height
T	°C	temperature
t	h	creep time
V	-	box volume
Vm	mm³/mm²	material volume
Vmc	mm³/mm²	core material volume
Vmp	mm³/mm²	peak material volume
Vv	mm³/mm²	void volume
Vvc	mm³/mm²	core void volume
Vvv	mm³/mm²	pit void volume
Vx		functional parameters (volume)
σ_l	MPa	principal stress
σ_a	MPa	nominal stress amplitude
σ_y	MPa	yield stress
σ_u	MPa	ultimate tensile stress
ε_B	-	strain at break
σ_{creep}	MPa	creep pre-strain stress
δ	-	box width
ε_1	-	principal strain
ε_a, ε_{ae}, ε_{ap}	-	total, elastic and plastic (ductile) strain amplitude respectively
ε_s	-	secondary creep strain
ε_{creep}	-	creep strain
ε_t	-	tertiary creep strain
ω	-	damage state parameter

Abbreviations:

CMM	coordinate measurement machine
EBM	enclosing boxes method
EBSD	electron backscatter diffraction
LAB	percentage of low angle boundaries
LCF	low-cycle fatigue
LED	light-emitting diode
LSM	least square method
NM	non-measured points
ROI	region of interest
RU	real unit
SEM	scanning electron microscope
SFE	stacking fault energy
SSE	sum squared error
RMSE	root-mean-square error

1. Introduction

Creep and fatigue damage development is a complex and difficult phenomenon to model [1]. This phenomenon results from the combination of two different failure mechanisms which individually can be a very complicated to understand because they are influenced by many factors. In fact, not only the manufacturing technology and material structure [2], but also the variability in temperature, the loading [3,4] or the environment conditions [5] can impressively influence the fatigue life of a structural element. Though the wide research on the subject, which goes on for almost two centuries, modeling these complicated influences continues to challenge scientists and engineers. The dependence between loading features and fatigue lifetime is often explained using stress-based [6], strain-based [7], or energy-based [8,9] approaches. Nevertheless, more research is needed to better identify the governing variables as well as to develop more accurate fatigue damage quantifiers [10-14].

Metallic materials are key materials for critical structural parts and mechanical components subjected to complex failure processes. In particular, aluminium alloys have showed to be preferable materials for specific engineering areas, due to their high strength, low density, and attractive price [15-17]. Creep-fatigue relations occur in many elements made of metallic alloys, in which quasi-static and transient load changes alternate or overlap. Sonntag et al. [18] investigate various stress relaxation and creep phases within each fatigue cycle. Hormozi [19] et al. introduced symmetrical hold time to the test and lead to find the interaction of creep/fatigue. They also employed energy density method to identify the cycle number at different stages. Sun et al. [20] form 3D damage diagram for estimating creep-fatigue damage level. Tomczyk and Seweryn [21] investigated EN-AW 2024 aluminum alloy under LCF loading with creep pre-strain. They determined and verified the damage growth model. However studies dealing with surface topography measurements in aluminium alloys caused by creep-fatigue damage are missing in the literature.

Thus, the development of surface topography measurement techniques opens new opportunities to analyze the failure mechanisms in many fields of science and industry [22] and to better understand the surface topography features. The fractured surface integrity assessment [23] based on this detailed analysis of fracture surfaces can consign precious information about the damage history of the post-mortem inspected element. In most cases, the fracture surfaces caused fatigue loading are so complex that not only height Sx or volumetric Vx parameters are used for their complete

description, but also other parameters not covered in the standards [24,25], such as the fractal dimension D_f [26,27].

The above-mentioned reasons were the motivation to undertake the research presented in this paper, wherein the thread of the metrological fractographic analysis and fatigue life modeling for the EN-AW 2024 AA subjected to creep pre-strain and LCF failure was combined.

2. Methodology

The complete testing procedure can be divided in three main stages. Firstly, creep tests at elevated temperature (100ºC, 200ºC, or 300ºC) are conducted. Then, LCF fatigue tests at room temperature (21°C) are performed. At last, the post-mortem fracture surfaces are measured with 3D Coordinate Measurement Machine (CMM). The data collected at all stages of this research allows for a detailed analysis of fatigue life, taking into account fractographic aspects.

2.1. Material and specimens

EN AW-2024 aluminum alloy in T3511 temper was obtained in the form of 16 mm-extruded rod. The chemical composition of the tested alloy is shown in Table 1. The cylindrical specimens had a gauge section with a length of 13 mm and diameter of 6.5 mm, respectively. Figure 1 shows the shape and dimension of the specimens. The differences in the geometry of the specimens concerned only the grip part. In the creep tests (see Fig. 1(a)), a thread was used in this part due to the method of fastening in the testing machine rods. It ensured stable fixation of the specimen at elevated temperature. The thread was 'removed' after pre-strain process, unloading and cooling of the specimen. This process was carried out using the technology of accurate turning. It should be emphasized that during machining, no loads were introduced in the gauge length of the specimen. Monotonic tensile tests were carried out before the start of the proper tests. Metallographic micro-sections were also made in order to observe the microstructure of the material. These tests confirmed that the properties of the material before and after thread removal are the same. The specimens prepared in this way were subjected to LCF tests (see Fig. 1(b)). The gripping part, devoid of thread, was clamped in the hydraulic jaws of the fatigue testing machine grips.

Table 1. Nominal chemical composition of the EN AW-2024 aluminum alloy (wt.%) [21].

Si	Fe	Cu	Mn	Mg	Cr	Zn	Ti	Al
0.13	0.25	4.4	0.62	1.7	0.01	0.08	0.05	92.76

a)   b)
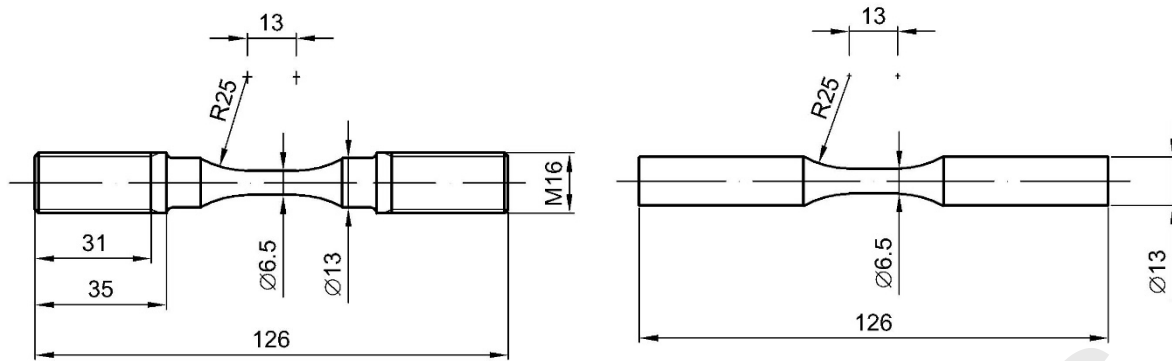
Fig. 1. Dimensions of specimens used in: (a) creep tests; (b) fatigue tests (units: millimeters).

The as-received material was characterized by Young's modulus E=74GPa, yield stress σ_y=447MPa, ultimate tensile stress σ_u=580MPa and strain at break ε_B=13.3%. The monotonic tensile curve of the tested batch is shown in Figure 2.
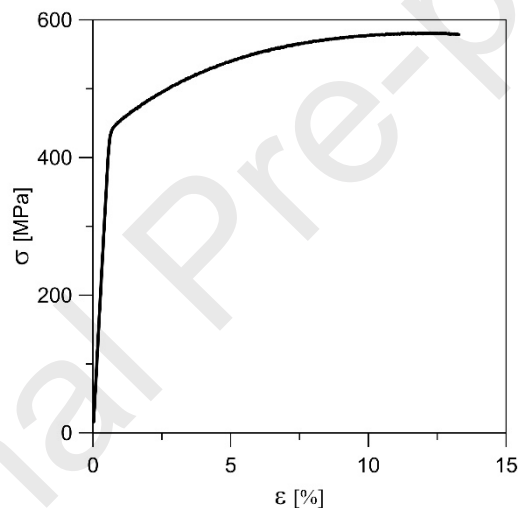

Fig. 2. Monotonic stress-strain tensile curve for the as-received material.

2.2. Creep tests

The creep tests were carried out on a four-column Kappa 100S machine with an electromechanical drive and loading range up to 100 kN, manufactured by Zwick/Roell. The test stand was equipped with an Epsilon extensometer, with a measurement base of 25 mm and a range of ±12.5 mm. The thermal loading was generated using a three-zone Maytec furnace with a dedicated Zwick/Roell controller and the specimen temperature was measured by thermocouples. The test stand (creep tester – furnace – controller) was managed using Testar Xpert II software. The creep tests were conduct according to the EN ISO 204 standard [29] considering three temperatures (100°C, 200°C, or 300°C) for five levels of strain at every temperature. For each temperature, two different strain values were defined. Full creep-rupture curves for conditions in which pre-strains were applied are shown in Fig. 3. These curves made it possible to determine the level of creep pre-strain (ε_s and ε_t) of the specimens at each elevated temperature.
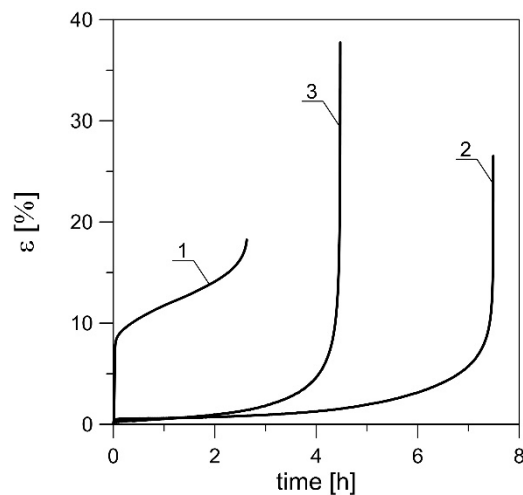
Fig. 3. Creep-rupture curves of analyzed material: 1 – T=100°C, σ_{creep}=530 MPa; 2 – T=200°C, σ_{creep}=279 MPa, 3 – T=300°C, σ_{creep}=92 MPa

The initial strain was applied in such a way that some of the specimens were subjected to creep at one of the three temperatures at a constant value of creep until reaching the pre-defined secondary creep strain (ε_s), and then unloaded, cooled, and subjected to low-cycle fatigue. Another batch of specimens was subjected to creep strain, called here tertiary creep strain (ε_t), and then the specimens were unloaded, cooled, and subjected to low-cycle fatigue. The σ_{creep} value for both levels of pre-strain at a given temperature was the same, as presented in Fig. 4(a) and in Table 2. A summary of the creep temperature T registered in the creep experiments for the above-mentioned creep strain levels and the planed LCF strain amplitudes (ε_a) is exhibited in Fig. 4(b).
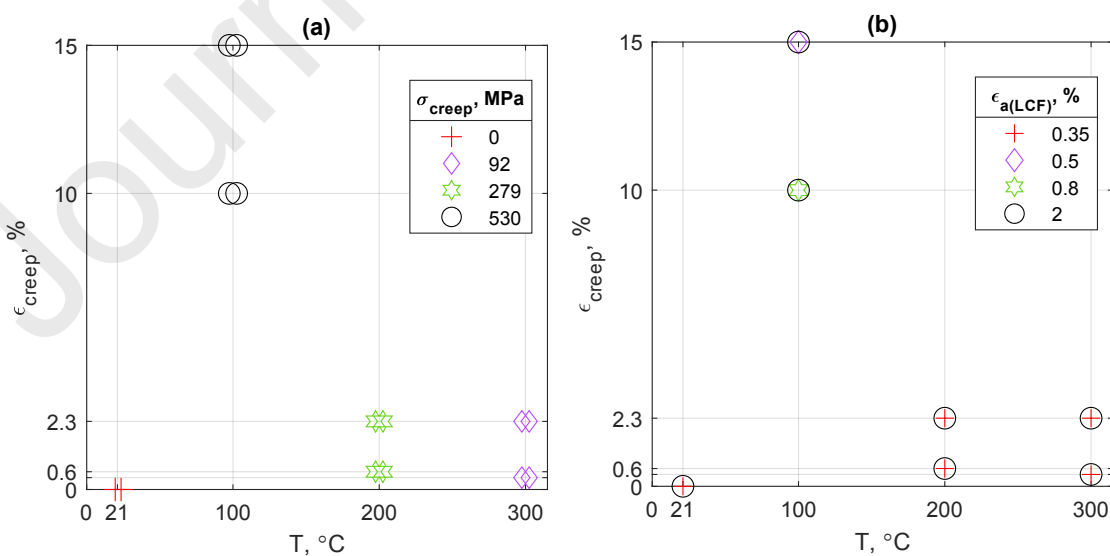
Fig. 4. Creep strain ε_{creep} and pre-strain temperature T, grouped by: (a) creep stress σ_{creep}; (b) LCF strain amplitude ε_a.

2.3. LCF tests

LCF tests were performed in an MTS 322 servo-hydraulic machine with an actuator range of ±50 kN, and the strain response was measured by using an extensometer with a gauge length of 12.5 mm and range of ±5 mm attached directly to the specimen. Cyclic loads were carried out with the control of the total strain amplitude ε_a. Strain ratio $R_\varepsilon=-1$, and load frequency $f=0.2$ Hz. Nominal stress values σ_a were determined for the mid-life cycle.
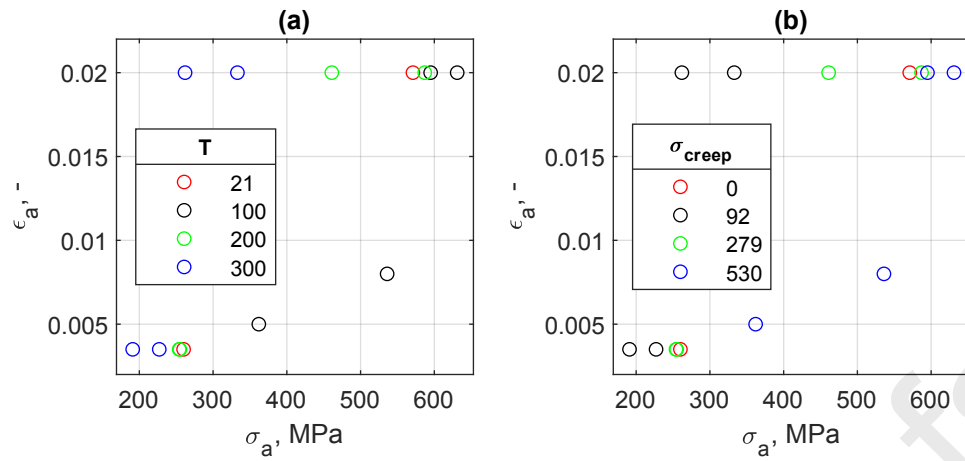
The applied strain amplitude (ε_a) and the corresponding stress amplitude (σ_a) for the different pre-strain temperatures (T) and stress-creep histories (σ_{creep}) are presented in Fig. 5. Fig. 6 shows the fatigue life curves for the as-received material and for the material with different pre-strain histories.[1] Total strain amplitude ε_a was determined here according to the Manson-Coffin-Basquin [30-32]:

$$\varepsilon_{\mathrm{a}} = \varepsilon_{\mathrm{ae}} + \varepsilon_{\mathrm{ap}} = \frac{\sigma_f'}{E}\left(2N_f\right)^{b_1} + \varepsilon_f'\left(2N_f\right)^{c_1},$$ (1)

where ε_{ae} and ε_{ap} are the elastic and plastic strain amplitudes, respectively; σ_f' and ε_f' are the fatigue strength and ductility coefficients, respectively; b_1 and c_1 are the fatigue strength and ductility exponents, respectively; and $2N_f$ is the number if reversals to failure. Results for $\sigma_{creep}=0$ and $T=21°C$ represent the tests conducted for the as-received condition, at room temperature, without the application of any pre-strain. Note the N_f values for low and high load amplitudes (see Tab. 2 and Fig. 6.). They clearly show that for large plastic deformations there is a substantial increase in the fatigue life of the material with pre-strain (in 200°C and 300°C) in relation to as-received material. However, in the case of small plastic deformations, the aforementioned fatigue life deteriorates. At the same time, in the case of pre-strain at 100°C, the fatigue life deteriorates for high strain amplitudes compared to as-received material.

Table. 2. Specimen nomenclature and pre-strain condition together with LCF condition.

| Specimen symbol	pre-strain condition			LCF condition		
	temperature T [°C]	ε_s or ε_t [%]	σ_{creep} [MPa]	ε_a [%]	σ_a [MPa]	N_f [cycles]
(1)	as-received material			0.35	571	58965
(2)				2	260	7
S4	100	ε_t=15	530	2	631	2
S5				0.5	362	5423
S88		ε_s=10		2	595	3
S1010				0.8	536	183
R3	200	ε_s=0.6	279	2	587	12
R6				0.35	254	62739
R77		ε_t=2.3		2	461	31
R11				0.35	255	22914
P7	300	ε_s=0.4	92	2	333	66
P3				0.35	227	5747
P55		ε_t=2.3		2	262	99
P1010				0.35	191	3836

Fig. 5. Strain-stress relationships for different pre-strain scenarios, grouped by: (a) pre-strain temperature *T*; (b) pre-strain stress σ_{creep}.

a)
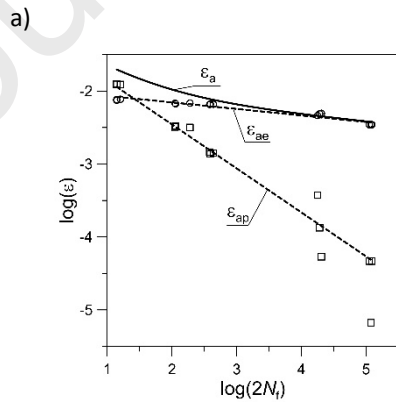
b)   c)
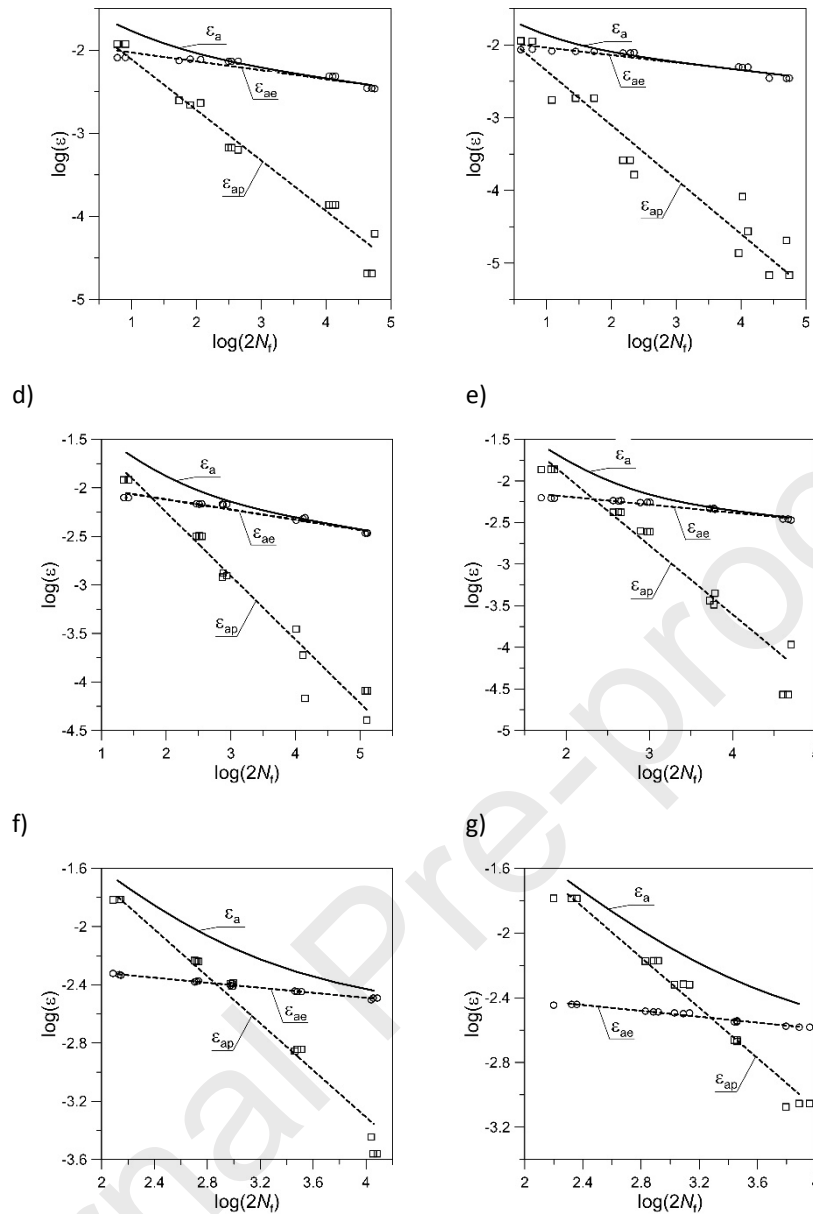
Fig. 6. Fatigue life curves at room temperature for the as-received material (a) and for material with different creep pre-strain histories: (b) T=100°C, σ_{creep}=530 MPa, ε_s=10%; (c) T=100°C, σ_{creep}=530 MPa, ε_t=15%; (d) T=200°C, σ_{creep}=279 MPa, ε_s=0.6%; (e) T=200°C, σ_{creep}=279 MPa, ε_t=2.3%; (f) T=300°C, σ_{creep}=92 MPa, ε_s=0.4%; (g) T=300°C, σ_{creep}=92 MPa, ε_t=2.3% [1]

2.4. Fracture surface topography measurement after LCF loading

The fracture surfaces of the analyzed specimens were examined by the 3D CMM, a Mitutoyo Quick Vision Apex 302, equipped with a 2× lens and programmable light-emitting diode (LED) stage and coaxial lighting. It was used a scale resolution of 0.1 µm with a linear encoder scale type. Topography data processing and calculations were done by means of MountainsMap surface metrology software.

According to the entire fracture surface method [33], the whole surface was reduced to eliminate the regions associated with the geometric discontinuities or missing points and to obtain uniform

dimensions for all samples. This way of selecting data for analysis was verified for different loading conditions, materials, and specimen shapes. In the case analyzed here, the entire fracture surface was reduced to a circle of 6 mm diameter, in order to remove the final break, discontinuities and "non-sampling" areas. The process of selecting the Region of Interest (ROI) is shown in Figure 7. The figure on the left-hand side exhibits the original fracture surface, while the other shows the ROI for the same specimen. This particular fracture surface belongs to the P3 specimen, which was subjected to pre-strain stress σ_{creep} of 92 MPa at a temperature T equal to 300°C, and next was tested in LCF regime at strain amplitude ε_a equal to 0.35% (see Table 2). The selected area is marked with a circle over the entire fracture surface shown on the left-hand side of Fig. 7, and the right-hand side displays the extract effect. Non-measured points (NM) are represented by the white color areas.
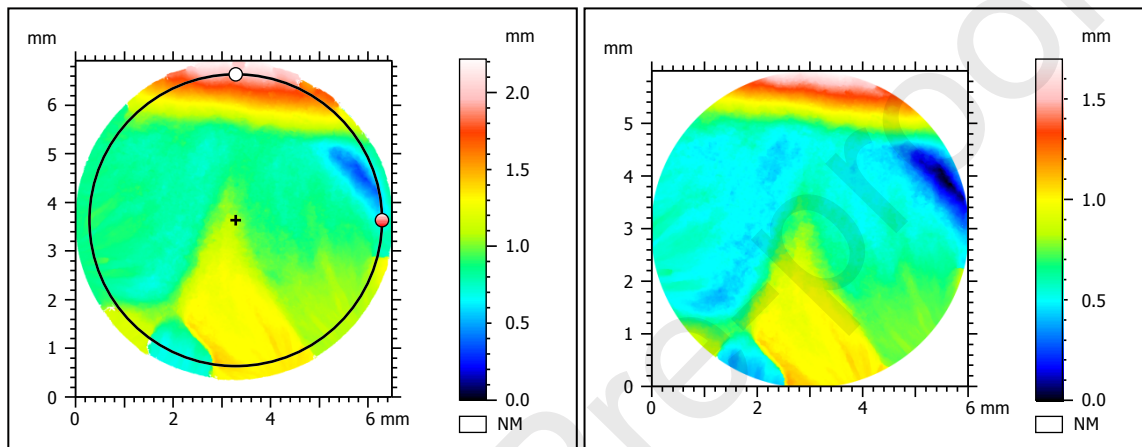

Fig. 7. Scheme of the extracted area – Region of Interest (ROI) of the P3 specimen.

Surface topography studies were carried out on the fracture area using both height parameters Sx, and volume parameters Vx, according to ISO 25178-2 standard [34]. This standard, whose main title is "Geometrical product specifications (GPS) - Surface texture: Areal", introduces the terminology and the main definitions associated with surface texture, and describes the main parameter used in the evaluation of surface texture. The examined surfaces were also characterised by fractal dimension D_f, measured by the Enclosing Boxes Method (EBM). In this approach, when the surface is divided, algorithms have to maintain the number of iterations that take place. The resolution of the plot defines the number of iterations and, therefore, the calculation time. In this analysis, for coarse resolution, it was 15 data points, and for extra-fine resolution, it was 96 data points. The EBM divides the area into smaller divisions with a width δ and calculates the volume ($V\delta$) of all volumes covering the entire area. This is an iterative procedure in which the width of the box is changed to $\ln(V\delta)/\ln(\delta)$. Despite a logarithmic scale is used for the axes, the values of the divisions are given as dimensional units. To estimate the fractal dimension D_f, a line is fitted using the Least Square Method (LSM). The absolute slope of the fitted line represents the value of the fractal dimension D_f.

Fig. 8 shows exemplary plots of fractal dimension determined for coarse resolution (see Fig. 8a, 8c and 8e) and extra-fine resolution (see Fig. 8b, 8d and 8f). This fracture surface belongs to the specimen *(1)* without pre-strain under LCF at a strain amplitude ε_a=0.35% (see Table 2). Morphological envelopes method (see Fig. 8e and 8f) embraces the upper and lower envelopes which are calculated by morphological opening and closing interposing a structuring element that is a horizontal line segment of length δ. The computed volume for surfaces ($V\delta$) is plotted as a function of the scale

ln($V\delta$)/ln(δ). The fractal dimension D_f is calculated from the slope of one of the two regression lines that corresponds better to the fitted data. In box counting, the real scale and the unit are unknown; thus, the surface is sampled using arbitrary values of V, and the unit of detail is deduced from the data after the calculation. Enclosing boxes in the real unit method (see Fig. 8c and 8d) are similar to the EBM but, in such a case, it uses boxes with a width in real size (instead of a width in points).
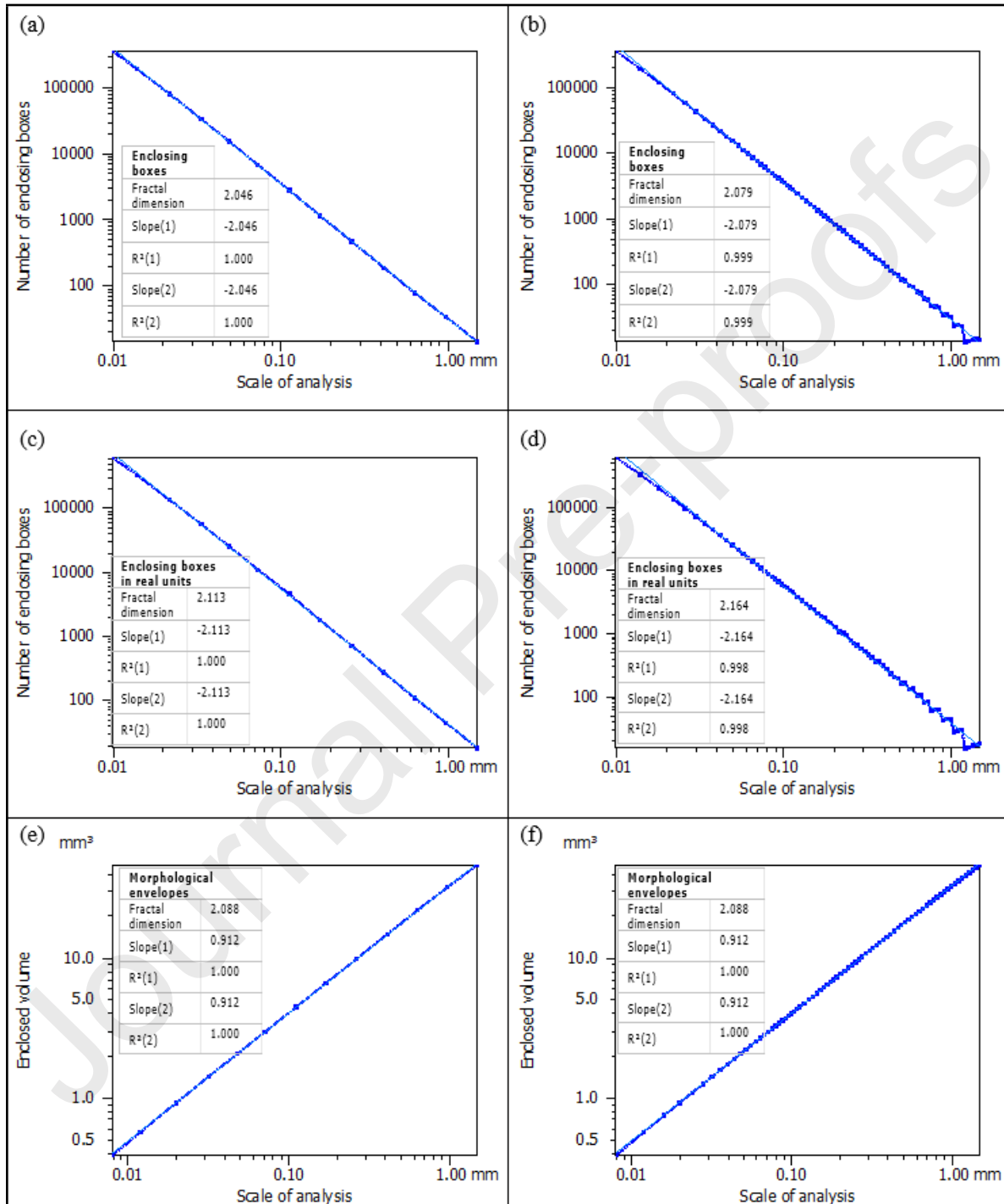
Fig. 8. Fractal dimension analysis for the specimen *(1)* extracted area using the entire fracture surface method: (a) enclosing boxes - coarse resolution; (b) enclosing boxes - extra-fine resolution; (c) enclosing boxes in real units - coarse resolution; (d) enclosing boxes in real units - extra-fine resolution; (e) morphological envelopes - coarse resolution; (f) morphological envelopes - extra-fine resolution.

3. Results and discussion

This section is organized into three subsections. The first one addresses the fracture surface topography features in terms of standard-based and fractal-based parameters and presents an overview of the creep pre-strain behaviour for the tested conditions. Next, fracture surfaces are examined by SEM to identify the main failure mechanisms and the surface morphologies. Finally, a new fractography-dependent model is developed to estimate the fatigue lifetime.

3.1. Fracture surface topography

The experimental LCF tests under creep conditions at elevated temperature for the EN AW 2024 aluminum alloy, as already mentioned in the previous section, was carried out in a previous paper [21]. However, in order to better understand the fracture surface morphology features and the associated damage accumulation phenomena, the cyclic deformation behaviour of the tested alloy after creep pre-strain conditions, is briefly described, see Figure 9. It was found that standard plots x- and y-coordinates using a base-10 logarithmic scale on the x-axis and the y-axis would be less appropriated, so the log-log scales were not used. Figure 9a shows the typical relationship between the applied strain amplitude and the fatigue life for different temperatures, while Figure 9b shows the relationship between the applied stress amplitude and the fatigue life for different creep stresses. In both cases, it is clear that both variables (i.e. temperature and creep stress) have a strong influence on fatigue life (see Fig. 9). This indicates that the development of fatigue life prediction models to deal with these two combined effects is a complex task.
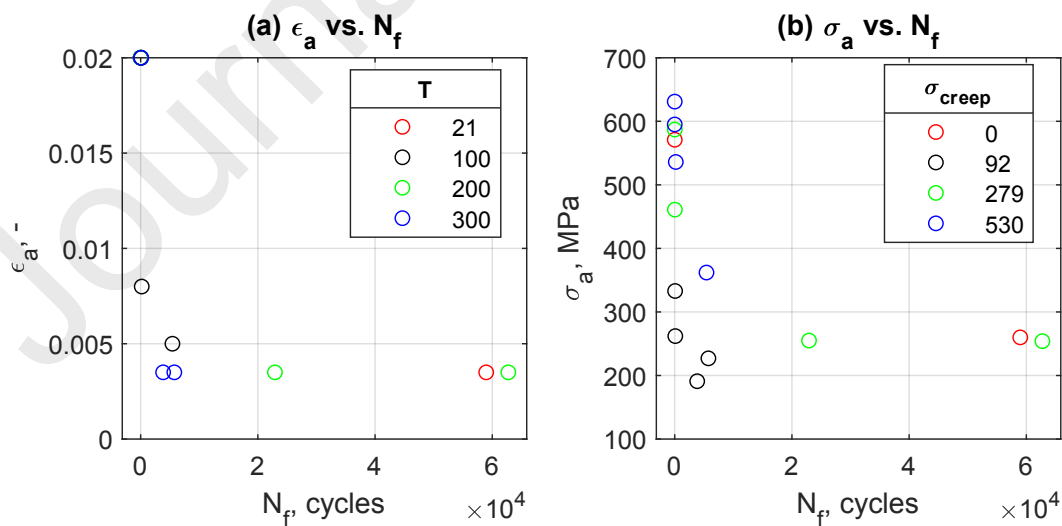
Fig. 9. Strain amplitude ε_a and stress amplitude σ_a versus fatigue life N_f after different pre-strain scenarios: (a) grouped by temperature T; (b) grouped by creep stress σ_{creep}.

Figure 10 displays the typical fracture surfaces obtained for 14 analysed cases. Amplification in the z-axis has been optimized (reduced) to facilitate the presentation of all fractures in a single 3D series view. Pseudo-color views show maximum values close to the surface (final fracture region) and also small values at the surface (initiation sites). Of course, it depends on which of the two parts of the split specimen we are considering. It also presents a table with the mean, standard deviation, and minimum and maximum values of fracture surface topography parameters [33], respectively. The three group of surface parameters shown in the table are: (1) height parameters expressed as the height function; (2) functional parameters (volume) calculated for a material ratio mr; and (3) functional parameters (stratified surfaces) based on a graphical construction of the Abbott-Firestone curve built from an areal surface. A summary histogram and the corresponding Abbott curves for all specimens are provided in the lower right corner of the same figure. Abbott curves seem to be similar for most of cases, notwithstanding individual histograms and Abbott curves for all samples are also presented in Appendix A1. The Abbott curves have the smallest scale on heights (less than 2 mm) for the R6 and P3 specimens. These specimens were selected because their number of cycles to failure N_f are rather different, amounting to 5747 and 62739, respectively. The largest range of scale on heights (above 6 mm) was found for the S1010 specimen, with a correspondingly smaller number of cycles to failure N_f equal to 183.

|		Mean	Std dev	Min	Max
Height parameters					
Sq	mm	0.883	0.330	0.246	1.399
Ssk		0.088	0.631	-0.964	1.488
Sku		2.898	0.787	1.952	4.688
Sp	mm	1.940	0.672	0.804	2.953
Sv	mm	2.207	0.846	0.629	3.889
Sz	mm	4.147	1.432	1.665	6.554
Sa	mm	0.709	0.277	0.192	1.195
Functional parameters (volume)					
Vm	mm³/mm²	0.030	0.012	0.003	0.048
Vv	mm³/mm²	1.212	0.493	0.352	2.091
Vmp	mm³/mm²	0.030	0.012	0.003	0.048
Vmc	mm³/mm²	0.828	0.383	0.173	1.430
Vvc	mm³/mm²	1.112	0.462	0.338	1.998
Vvv	mm³/mm²	0.100	0.047	0.012	0.171
Functional parameters (stratified surfaces)					
Sk	mm	1.580	1.155	0.283	4.208
Spk	mm	0.882	0.440	0.062	1.403
Svk	mm	1.051	0.601	0.089	2.038
Smrk1	%	18.623	10.602	1.586	35.107
Smrk2	%	82.015	10.832	56.284	97.994

Fig. 10. 3D series view of the fracture surfaces with summary list of main parameters, height histogram and Abbott curves.

The surface topography parameters Sx and Vx, and especially Sq and Vv, which were previously selected as the best fitting parameters [36], are later used for fatigue life assessment. The Sq parameter, which is the standard deviation, has more statistical significance. This height parameter is directly related to surface energy. The void volume parameter Vv is calculated by integrating the volume enclosed above the surface and below a horizontal cutting plane. In this study, based on the performance algorithms and specific calculations used for estimating the fractal dimension D_f, the most appropriate method of fractal analysis for the investigated surfaces was the morphological envelope. The resulting envelope follows the form of the surface all over in a way that the distortions caused the end effects are avoided. The morphological envelope method requires more computation time than EBM, but for the purposes of this paper it is negligible. All the results of the fracture surface topography parameters are exhibited in Table 3. The columns with the parameters of the surface topography of fatigue fractures (Sq, Vv, and D_f) which were used for further analysis and presented in the discussion are marked in green.

Table 3. Summary of the *Sx, Vx* and *D$_f$* results.

Specimen	height parameters, *Sx*							functional parameters (volume), *Vx*						fractal dimension, *D$_f$*				
	Sq	Ssk	Sku	Sp	Sv	Sz	Sa	Vm	Vv	Vmp	Vmc	Vvc	Vvv	Morphological envelopes	EBM (coarse)	EBM (fine)	EBM (RU, coarse)	EBM (RU, fine)
P1010	0.799	0.535	2.632	1.955	1.922	3.877	0.654	0.029	1.297	0.029	0.644	1.229	0.068	2.085	2.033	2.056	2.103	2.146
P55	1.27	-0.054	2.284	2.746	2.746	5.492	1.034	0.041	1.771	0.041	1.287	1.644	0.127	2.049	2.002	2.018	2.145	2.17
P3	0.251	1.104	4.599	1.016	0.681	1.697	0.195	0.02	0.353	0.02	0.175	0.338	0.015	2.169	2.136	2.17	2.156	2.193
P7	0.755	-0.949	2.478	0.814	1.894	2.708	0.654	0.003	0.64	0.003	0.891	0.542	0.098	2.106	2.07	2.104	2.059	2.099
R11	0.784	-0.023	3.237	1.803	2.105	3.907	0.568	0.029	1.197	0.029	0.528	1.063	0.135	2.112	2.076	2.109	2.152	2.19
R77	0.689	0.563	3.248	1.973	2.102	4.076	0.522	0.034	1.102	0.034	0.493	1.023	0.08	2.075	2.031	2.071	2.118	2.166
R6	0.348	1.475	4.669	1.309	0.542	1.851	0.274	0.031	0.531	0.031	0.232	0.52	0.011	2.128	2.088	2.113	2.11	2.143
R3	0.883	-0.025	2.72	1.932	2.332	4.263	0.68	0.028	1.303	0.028	0.751	1.182	0.121	2.075	2.029	2.062	2.226	2.263
S1010	1.241	-0.209	2.367	2.681	3.912	6.593	1.003	0.041	1.658	0.041	1.301	1.524	0.133	2.061	2.015	2.052	2.133	2.17
S88	1.091	-0.166	2.786	2.312	2.696	5.009	0.839	0.034	1.569	0.034	0.892	1.396	0.172	2.079	2.038	2.069	2.128	2.159
S5	0.619	-0.31	2.625	1.463	1.568	3.031	0.497	0.031	0.726	0.031	0.68	0.666	0.06	2.135	2.098	2.133	2.136	2.175
S4	1.397	0.241	1.952	2.96	3.036	5.996	1.194	0.036	2.088	0.036	1.432	1.996	0.092	2.079	2.027	2.051	2.141	2.173
(1)	0.987	-0.716	2.271	1.313	2.441	3.754	0.849	0.009	1.035	0.009	1.126	0.917	0.118	2.088	2.046	2.079	2.113	2.164
(2)	1.202	-0.177	2.75	2.813	2.873	5.686	0.925	0.048	1.657	0.048	1.133	1.498	0.159	2.065	2.027	2.058	2.133	2.167
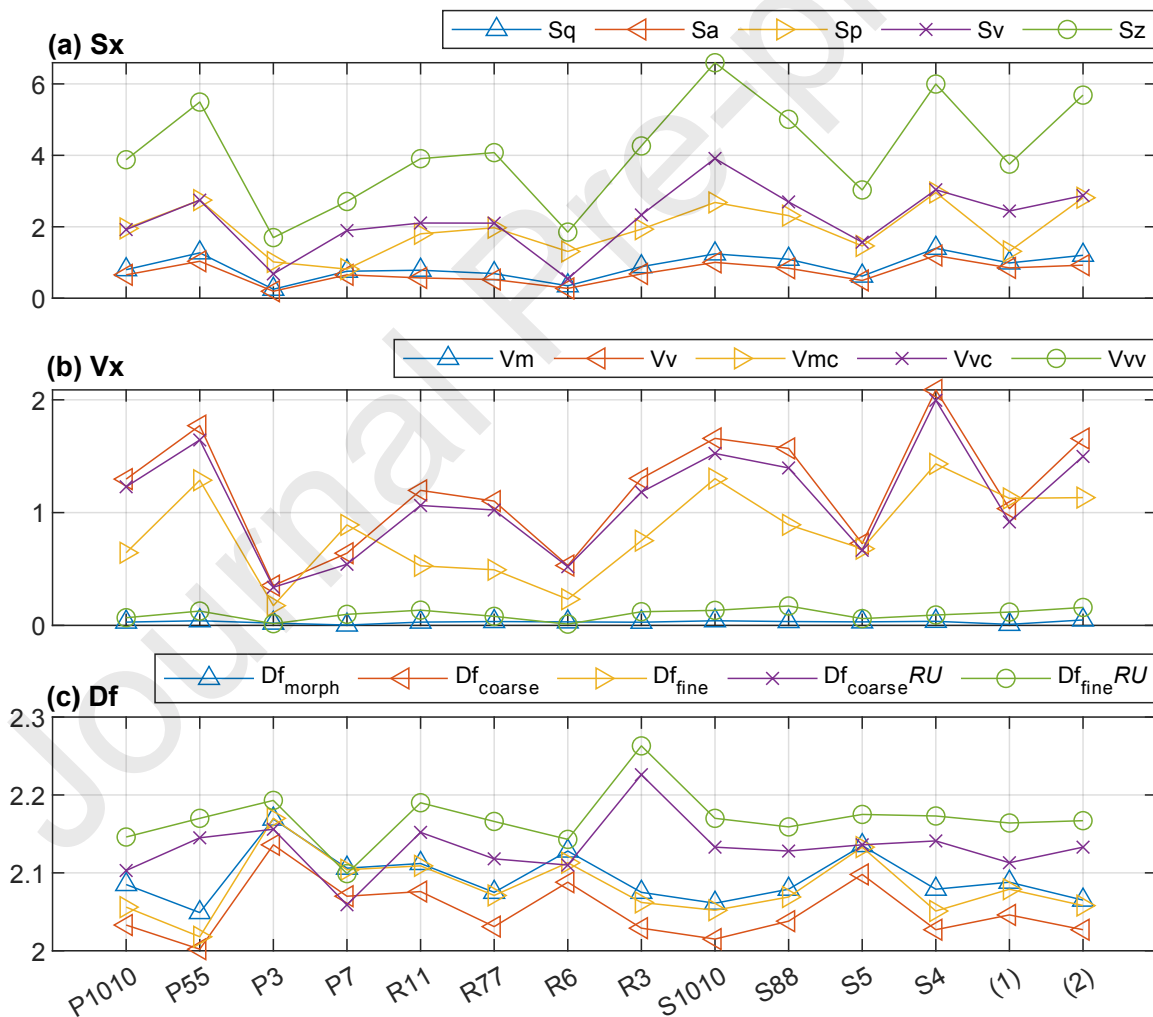
Fig. 11. Results of fracture surface topography measurement: (a) height parameters, *Sx*; (b) functional parameters (volume), *Vx*; (c) fractal dimension *D$_f$*. The units for each parameter are defined in the Nomenclature section.

The results of the fracture surface topography measurements for the tested specimens are presented in Figure 11. Figure 11(a) plots the *Sx* parameters, Figure 11(b) plots the functional parameters *Vx*, and Figure 8(c) plots the fractal dimension D_f. For most *Sx* parameters, the maximum value is for specimen S1010, and the minimum for P3 (see Fig. 11(a)). Regarding the *Vx* parameters, the maximum value was found in the majority of cases for S4 while the minimum value was found for the P3 fracture surface, similarly to the *Sx* parameters. For the fractal dimension D_f, determined by the method of morphological envelopes, which was considered the most adequate, the maximum value occurred for the P3 topography, and was equal to 2.169, while the minimum value occurred for P55 specimen, and was equal to 2.049 (see Fig. 11(c)).

Figure 12 displays, on each boxplot, the median value (central red line) and the 25th and 75th percentile values (bottom and top edges of the box, respectively) found in the analysis. The whiskers extend to the most extreme data points not considered outliers, and the outliers are plotted individually using the '+' marker symbol. Among the *Sx* parameters, *Sz* has the largest numerical range of results, which of course results from the way it is calculated (maximum height). Root mean square height *Sq* and arithmetical mean height *Sa* has lower intervals, with the first parameter being more statistically significant. Among the *Vx* parameters, void volume has the largest range of values. *Vv* can be used to describe surface shape and distinguish surface volume characteristics with different roughness levels. As far as the fractal dimension is concerned, it is clear from Fig. 12(c) that higher resolutions result in increased values. Furthermore, all the samples had a relatively small scatter irrespective of the calculation method. The differences in the D_f values varied from 2.002 (enclosing boxes considering the coarse approach) to 2.263 (enclosing boxes in real units considering fine resolution).
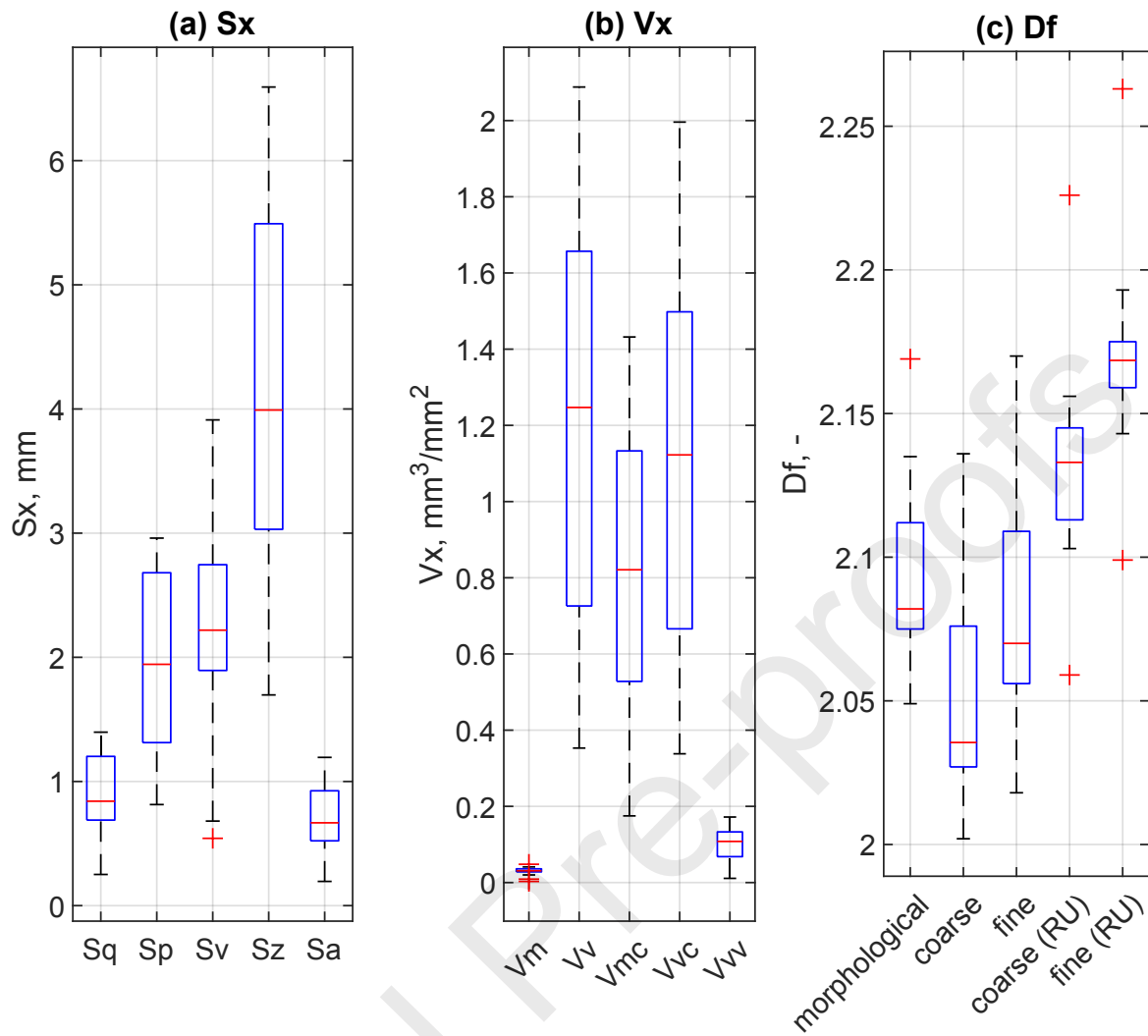
Fig. 12. Boxplot: (a) height parameters, *Sx*; (b) functional parameters (volume), *Vx*; (c) fractal dimension, D_f.

Surface topography is the consequence of the simultaneous interactions of many independent factors, both random and determined, and as an outcome, these interactions lead to a very complex geometry. There are evident differences between individual fractures, as shown in Figure 13, if we compare mixed creep and LCF histories. Although there are obvious differences between specific fracture zones, the methodology proposed here, called entire fracture surface method, treats the fractured surface as a total area, not distinguishing the specificities of these individual regions (e.g. crack initiation, crack propagation, or final rupture).

The directivity of the geometric structure of the surface depends on the fracture causes and it results from the kinematics of the fracture process. The isotropy of a medium is generally based on the fact that it exhibits the same physical or geometric properties in all directions. The isotropy of a surface, therefore, means that the surface has the same structure in all directions. It is also a perfectly symmetrical structure with respect to all possible axes of symmetry. In the examined case, the isotropy was determined by analyzing the autocorrelation function. Texture isotropy assesses the directionality and the periodicity of surface having periodic motifs in two directions (see upper right corner of each of the fractures in Fig. 13).

Extreme values of isotropy occur for the fracture surfaces of specimens R6 and R77. For the R6 fracture, the shape of texture isotropy function is asymmetric, slender, and elongated in one direction for anisotropic surfaces. The isotropy in this case was approximately 21%. On the other hand, the circular and symmetrical function graph for isotropic surfaces reached the isotropy value of almost 78% (see Fig. 13, specimen R77).
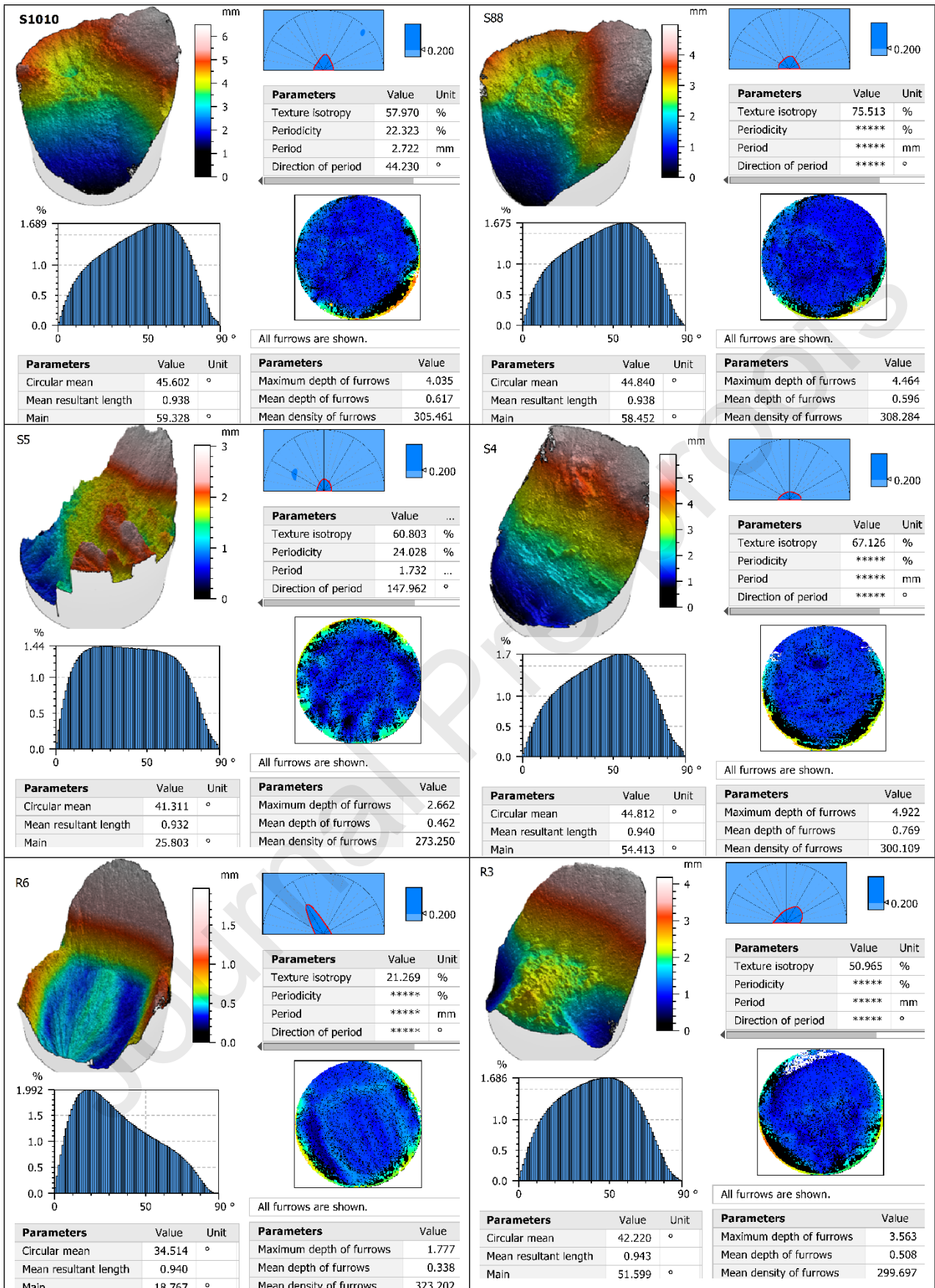
In addition to the 3D view of the fractures and the aforementioned texture isotropy, in the lower part of each case, on the left-hand side, respectively, we can see the slope distribution and furrows. Slope distribution functions in MountainsMap software analyze slope and orientation of all triangular tiles composing the surface and present their distribution. Polar angle is divided on 90 bins and width of each bin is 1°, whereas furrows analyze parameters concerning the micro-valleys network, such as the depth and the density.

Slope distribution and orientation of all triangular tiles formulating the surface with their computed values presented in histograms have a front-side distributions (see Figure 13). P3 and R6 fractures are an exception and have left-side concentrated distributions. The highest value for the circular mean parameter was found for the surface of specimen (2) for a 47.515° orientation, whereas the lower value (32.390°) was associated with the P3 fracture. The mean resultant length parameter has a value greater than 0.9 for all surfaces. Moreover, the main parameter has the highest value for the S1010 surface (59.320°), whereas the minimum value was found for the P3 specimen (16.585°).

Furrow renderings (see Fig. 13) were obtained through Fourier transform applied by using MountainsMap software on topographic height functions that simulate furrows about peaks and valleys along the surface for better qualitative visualization of the fracture surface morphology. The results of Table 4 indicate that the values of the maximum depth of furrows are smaller for the creep temperature T=300°C than for the T=100°C and constitute their part expressed as a percentage, respectively 26.1% for maximum depth of furrows, 36.6% for mean depth of furrows and 84.5% for mean density of furrows.

Specimen 1:

Parameters	Value	Unit
Texture isotropy	33.315	%
Periodicity	*****	%
Period	*****	mm
Direction of period	*****	°

Parameters	Value	Unit
Circular mean	40.686	°
Mean resultant length	0.934	
Main	26.436	°

All furrows are shown.

Parameters	Value
Maximum depth of furrows	3.210
Mean depth of furrows	0.398
Mean density of furrows	289.636

Specimen 2:

Parameters	Value	Unit
Texture isotropy	34.144	%
Periodicity	*****	%
Period	*****	mm
Direction of period	*****	°

Parameters	Value	Unit
Circular mean	47.515	°
Mean resultant length	0.945	
Main	58.080	°

All furrows are shown.

Parameters	Value
Maximum depth of furrows	4.190
Mean depth of furrows	0.726
Mean density of furrows	291.712

S1010

Parameters	Value	Unit
Texture isotropy	57.970	%
Periodicity	22.323	%
Period	2.722	mm
Direction of period	44.230	°

Parameters	Value	Unit
Circular mean	45.602	°
Mean resultant length	0.938	
Main	59.328	°

Parameters	Value
Maximum depth of furrows	4.035
Mean depth of furrows	0.617
Mean density of furrows	305.461

All furrows are shown.

S88

Parameters	Value	Unit
Texture isotropy	75.513	%
Periodicity	*****	%
Period	*****	mm
Direction of period	*****	°

Parameters	Value	Unit
Circular mean	44.840	°
Mean resultant length	0.938	
Main	58.452	°

Parameters	Value
Maximum depth of furrows	4.464
Mean depth of furrows	0.596
Mean density of furrows	308.284

All furrows are shown.

S5

Parameters	Value	...
Texture isotropy	60.803	%
Periodicity	24.028	%
Period	1.732	...
Direction of period	147.962	°

Parameters	Value	Unit
Circular mean	41.311	°
Mean resultant length	0.932	
Main	25.803	°

Parameters	Value
Maximum depth of furrows	2.662
Mean depth of furrows	0.462
Mean density of furrows	273.250

All furrows are shown.

S4

Parameters	Value	Unit
Texture isotropy	67.126	%
Periodicity	*****	%
Period	*****	mm
Direction of period	*****	°

Parameters	Value	Unit
Circular mean	44.812	°
Mean resultant length	0.940	
Main	54.413	°

Parameters	Value
Maximum depth of furrows	4.922
Mean depth of furrows	0.769
Mean density of furrows	300.109

All furrows are shown.

R6

Parameters	Value	Unit
Texture isotropy	21.269	%
Periodicity	*****	%
Period	*****	mm
Direction of period	*****	°

Parameters	Value	Unit
Circular mean	34.514	°
Mean resultant length	0.940	
Main	18.767	°

Parameters	Value
Maximum depth of furrows	1.777
Mean depth of furrows	0.338
Mean density of furrows	323.202

All furrows are shown.

R3

Parameters	Value	Unit
Texture isotropy	50.965	%
Periodicity	*****	%
Period	*****	mm
Direction of period	*****	°

Parameters	Value	Unit
Circular mean	42.220	°
Mean resultant length	0.943	
Main	51.599	°

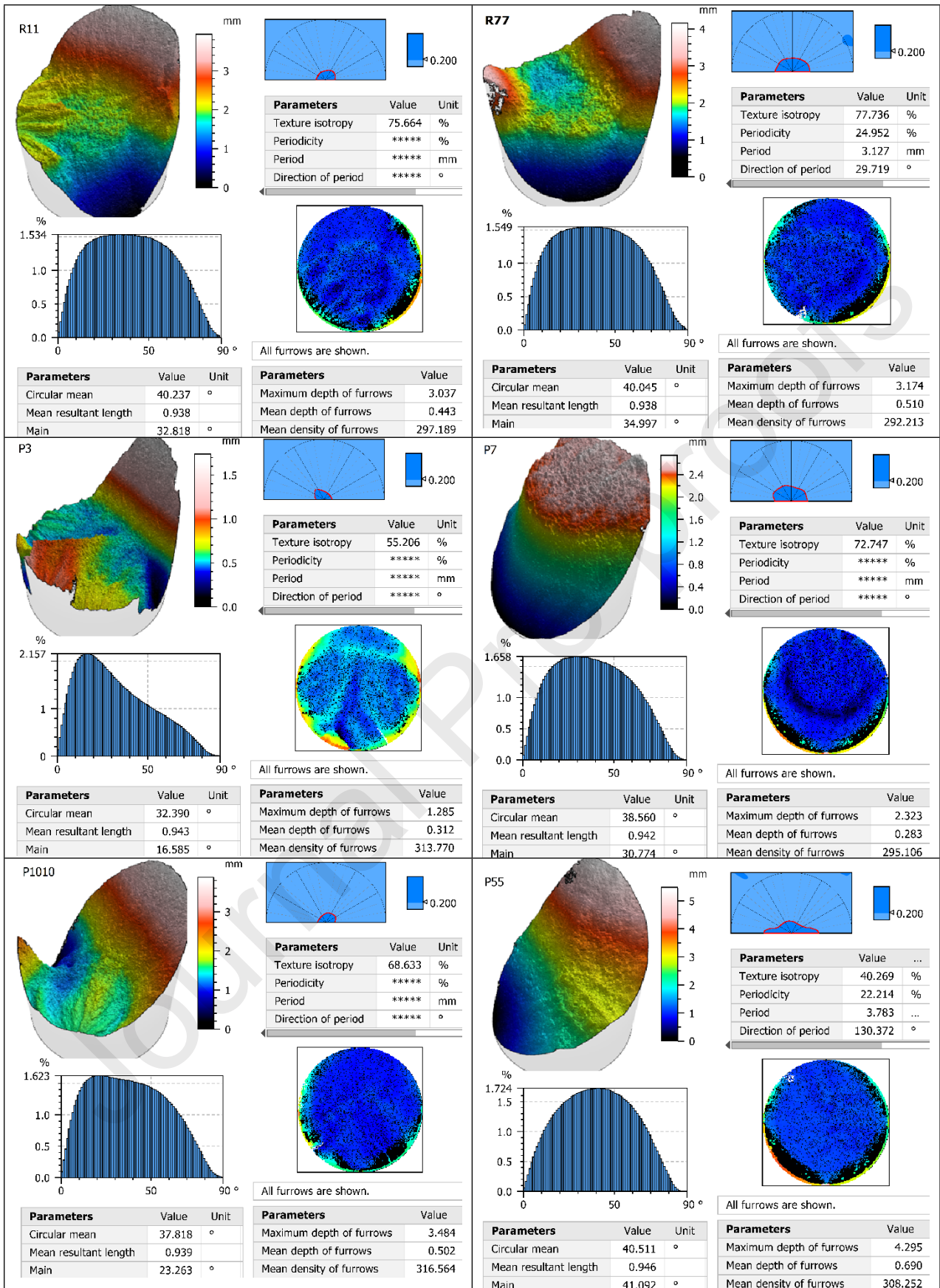| Parameters	Value
Maximum depth of furrows	3.563
Mean depth of furrows	0.508
Mean density of furrows	299.697

All furrows are shown.

Fig. 13. Entire fractured surface 3D views, texture isotropy, slope distribution and furrows parameters.

Table 4. Results for maximum furrow depth, mean furrow depth, and furrows' mean density.

Parameters	Specimen	Value	Unit
Maximum depth of furrows (MAX)	S4	4.922	mm
Maximum depth of furrows (MIN)	P3	1.285	mm
Mean depth of furrows (MAX)	S4	0.769	mm
Mean depth of furrows (MIN)	P7	0.283	mm
Mean density of furrows (MAX)	R6	323.202	cm/cm^2
Mean density of furrows (MIN)	S5	273.250	cm/cm^2

3.2. Failure mechanisms

To investigate the creep effects on both fatigue life N_f and the fracture surface topography, in terms of the entire fracture surface, it is important to analyze the failure mechanisms and material microstructure in individual fracture zones. Electron backscatter diffraction (EBSD) maps representing the material's microstructure evolution were conducted using a Hitachi SU70 scanning electron microscope (SEM). Surface tests of fractures after LCF tests were carried out using the Olympus SXD110 optical microscope and the Phenom XL scanning electron microscope.
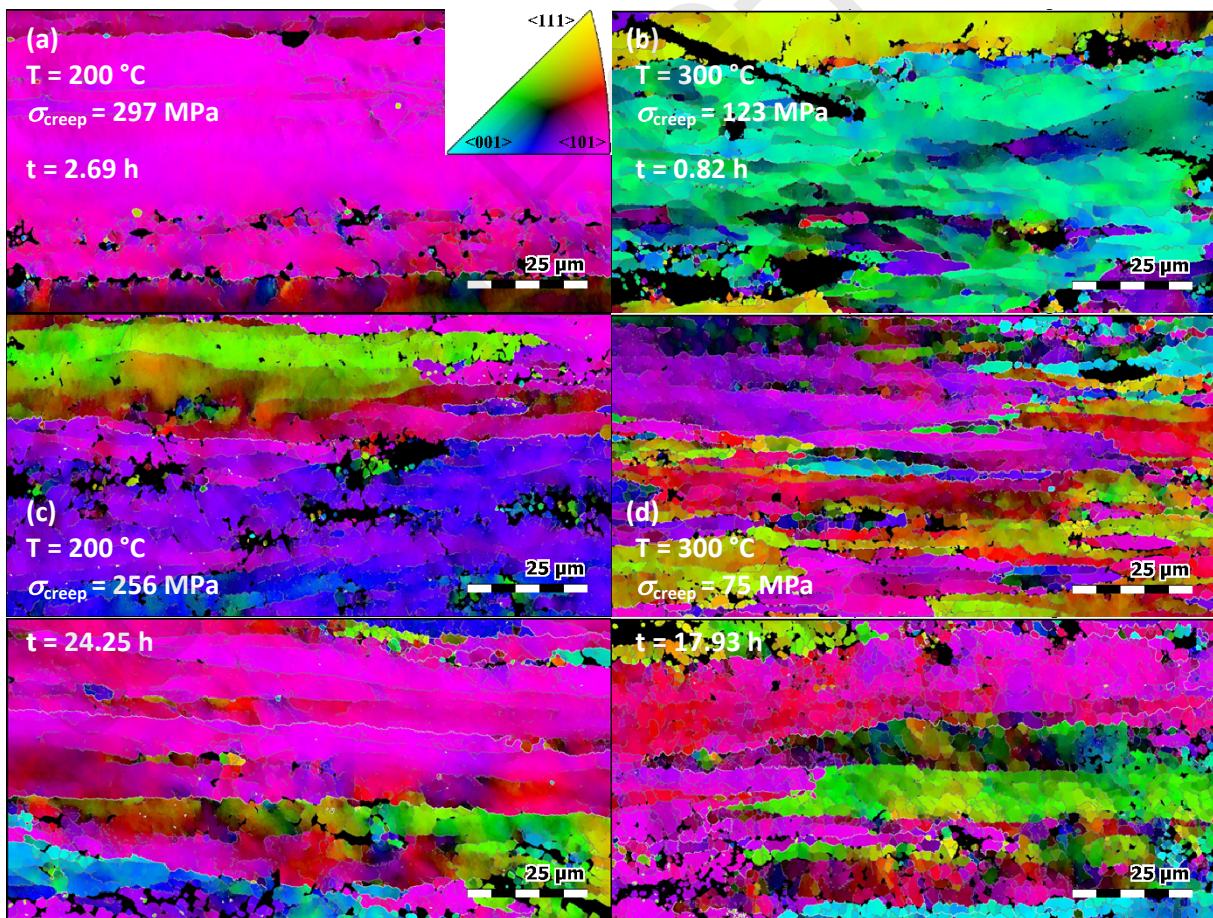
Fig. 14. Grain boundary misorientation maps for different creep-rupture test conditions [21]

Figure 14 shows the evolution of the microstructure of the tested alloy in the process of creep rupture for different stress values σ_{creep}, and thus different values of creep rupture time at temperatures of 200°C (Fig. 14a,c,e), and 300°C (Fig. 14b,d,f), respectively. The direction of the loading is horizontal here. It can be clearly observed large and elongated primary grains in the direction of the axis of the specimen. The white (light grey) lines represent boundaries with an angle of misorientation greater than 15°. The darker gray color corresponds to the boundaries with a low misorientation angle (LAB), i.e. 3-15°.

The material for which the creep time was the greatest (Fig. 14e and 14f) is characterized by a significant developed substructure of this type boundaries. It can be distinguished borders arranged in accordance with the axis of fibers (grains) and in a random way. In the case of samples with the shortest creep time (Fig. 14a and 14d), LABs also form such systems, but their density is clearly lower. For long creep times, partial (for 200°C) or almost complete (for 300°C), recrystallization of the microstructure can be observed. The resulting new grains soften the material.

Significant fragmentation, i.e. formation of fine grains, as a result of the recrystallization process is clearly visible, especially in Fig. 11f. A very well-developed structure of boundaries with a low misorientation angle (gray lines) is visible in this case. The shape of the grains is close to equiaxial. The formation of these grains is the result of dislocation rearrangement, and annihilation and is characteristic of materials with high stacking fault energy (SFE) [37,38].

A clear increase in the share of low-angle boundaries (LAB) was observed, as the creep time t_{creep} increased, and the creep stress σ_{creep} decreased. For the 200°C case, it increased from 78% for the shortest creep time to 95% for the longest. During creep at 300°C, the increase was not significant, it varied from 86% to 95%. Moreover, an increase in the creep time to failure leads to larger grains in the microstructure of the material [21].

Observation of the surface of fatigue fractures (Fig. 15, and Fig. 16) made it possible to identify the main mechanisms of failure. In the case of lower values of strain amplitude ε_a, the fracture surface is bi-planar in its nature. A certain (central) part is usually occupied by an area perpendicular to the load direction with a visible crack propagating from the external surface of the sample towards the longitudinal axis. At the same time, in the central part of the section, an area covered with numerous remnants of pores can be seen. The final failure was determined by the gradual tearing of the bridges between pores, followed by rapid shearing along the planes of maximum shear stresses. This is evidenced by the existence of a second (external) area inclined at an angle of 45°.

In the case of higher values of the control variable ε_a, the fracture surfaces also exhibit a bi-planar nature, but they clearly differ from the breakthroughs corresponding to small values of ε_a. The main difference concerns the lack of a visible crack propagating from the external surface of the sample. Here, the damage initiation process started in the central part of the cross-section perpendicular to the load direction. The shape and morphology of the dimples, i.e. the remnants pore (see Fig. 16), as well as earlier numerical calculations [39] carried out for static load, proved that the initiation was governed by the principal stress σ_i, or principal strain ε_i, acting in the axis of the sample. The bridges between the pores in this area were torn first. In the bottoms of the pores, coarse precipitations with sharp edges can be seen. At the moment of deformation, in the direction of the load, the bridge wall was in contact with the sharp edge of the precipitates, which could initiate the tearing process.

The second plane of the fracture surface, oriented at an angle of 45°, indicates the dominance of maximum shear stresses. This is also confirmed by the remnants of pores sheared in the

aforementioned direction, as well as by the view of cut smooth surfaces by cleavage planes. The shearing process was rapid, probably in one or several of the last cycles. It is worth noting that although the entire surface of the fractures of samples S4 and P55 is clearly inclined at an angle of 45°, the damage initiation took place exactly in the axis of the sample. Then, a shearing process occured rapidly.

Pre-strain temperature	Pre-strain level (ε_s or ε_t) [%]	Lower loading amplitudes	Higher loading amplitudes
as-received		(1)	(2)
100°C	ε_s=10	S1010	S88
	ε_t=15	S5	S4
200°C	ε_s=0.6	R6	R3
	ε_t=2.3	R11	R77
300°C	ε_s=0.4	P3	P7
	ε_t=2.3	P1010	P55

Fig. 15. View of fatigue fractures obtained for as-received material and for different creep pre-strain histories considering lower and higher values of strain amplitude ε_a.
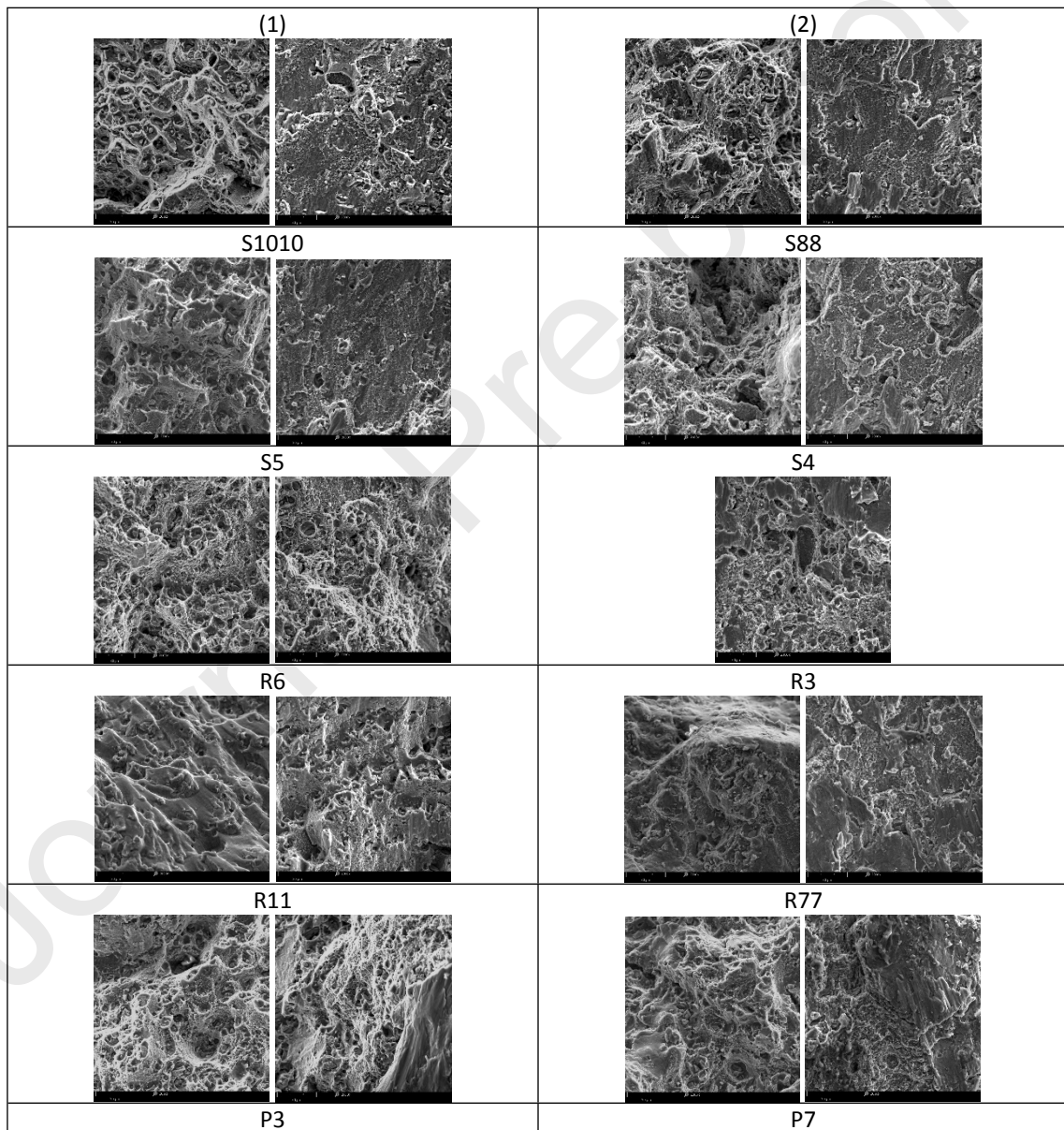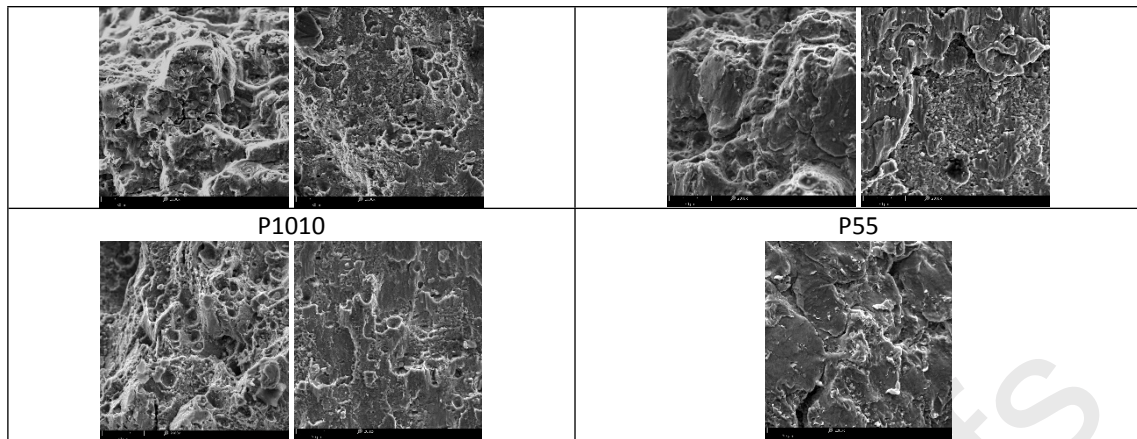
Fig. 16. SEM view of fatigue fractures presented in Fig. 15 for both central (ruptured) and external (sheared) parts of the fracture area. The figure on the left, inside each single table cell, corresponds to the central area, while the figure on the right corresponds to the external area. One image per cell means that the central and external areas did not differ in their morphology.

3.3. Fatigue life prediction

The fatigue life prediction models that relate the damage accumulation to the number of cycles taking into account the loading conditions based on the stress amplitude σ_a and the strain amplitude ε_a are difficult to establish in this case, see Fig. 17, due to the complexity of the various damaging mechanisms acting on the specimen. For Figure 17, as for plots in Figure 9, the log-log scale was abandoned. Curve fitting applied to both σ_a vs. N_f plot and ε_a vs. N_f plot, using a two-term exponential model, are shown in Figure 17a and Figure 17b, respectively. Fitted data show a satisfactory correlation, but it is not possible to properly model the fatigue life using them, taking into account the accompanying phenomena.

(a) σ_a vs. N_f

(b) ϵ_a vs. N_f
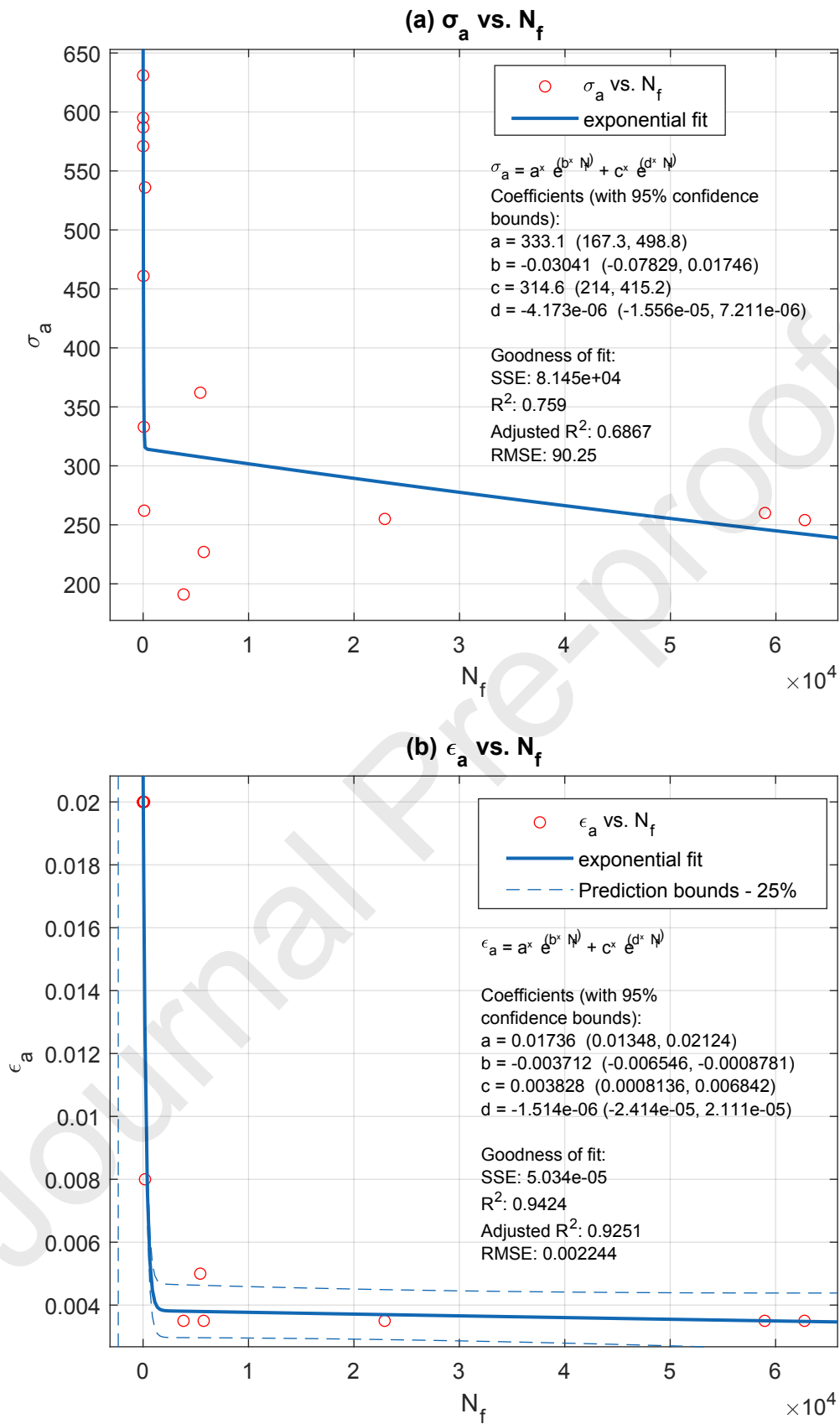
Fig. 17. (a) Stress amplitude σ_a vs. number of cycles to failure N_f; and (b) strain amplitude ε_a vs. number of cycles to failure N_f, using a two-term exponential model fit.

Fig. 18 analyses the relationship between the fracture surface parameters (Sq, Vv and D_f) and the fatigue life N_f. It is clear from these three plots that those parameters and the fatigue life N_f do not show satisfactory consistency in terms of linear functions for all tested specimens. Therefore, in the subsequent analysis, a combined model encompassing various parameters is used. The general tendency found from Fig. 18 is that the smaller the fatigue life N_f, the greater the roughness represented by Sq and Vv. The opposite tendency occurs for the fractal dimension D_f (see Fig. 18c).
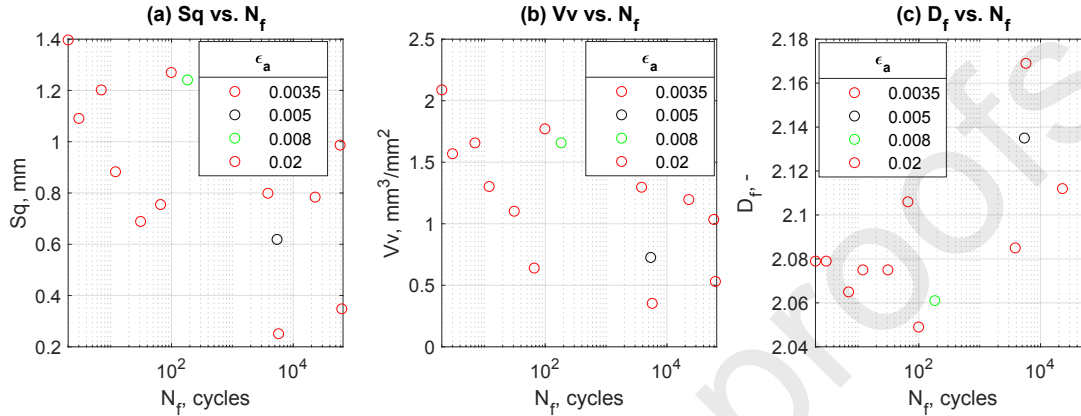
Fig. 18. Relationship between the selected fracture surface parameters and the fatigue life N_f, taking into account LCF strain amplitudes ε_a; (a) Sq versus N_f; (b) Vv versus N_f; (c) D_f versus N_f.

Due to the complexity of damage mechanisms, it is fundamental to identify adequate driving parameters for mixed creep under LCF along with fracture surface parameters to better assess the fatigue life N_f. Thus, in this study, the fatigue life is assessed via the novel fracture surface state parameter P, defined by the following expression:

$$P = \frac{Vv\, D_f}{Sq}\varepsilon_a\, \sigma_a + \varepsilon_{creep}\, \sigma_{creep} \qquad (2)$$

which combines the three topography characteristics (i.e. height parameter Sq, the functional parameter Vv, and the fractal dimension D_f) with both the strain amplitude ε_a and the stress amplitude σ_a, as well as the creep strain ε_{creep} and the creep stress σ_{creep}.

This parameter aims to reflect both low-cycle fatigue and the creep histories. Thus, the second part of the formula combines two main quantities in order to reflect the physical meaning of the damaging process. The first quantity reflects the low-cycle fatigue loading history by accounting for both the strain energy density ($\varepsilon_a\, \sigma_a$) [40-42] and the fracture surface energy through the combination of three fracture surface topography parameters ($V_v\, D_f$)/S_q. The second quantity reflects the creep scenario, and because fracture does not occur in this stage, only the strain energy density component is calculated.

Fig. 19 plots the proposed topographic stress factor P against the number of cycles to failure in natural logarithmic coordinates, log(N_f). An exponential function obtained from the data points is also plotted. Through the value of the coefficient of determination R^2, it can be observed a good correlation for this data configuration. Goodness of fit is shown in Fig. 19.
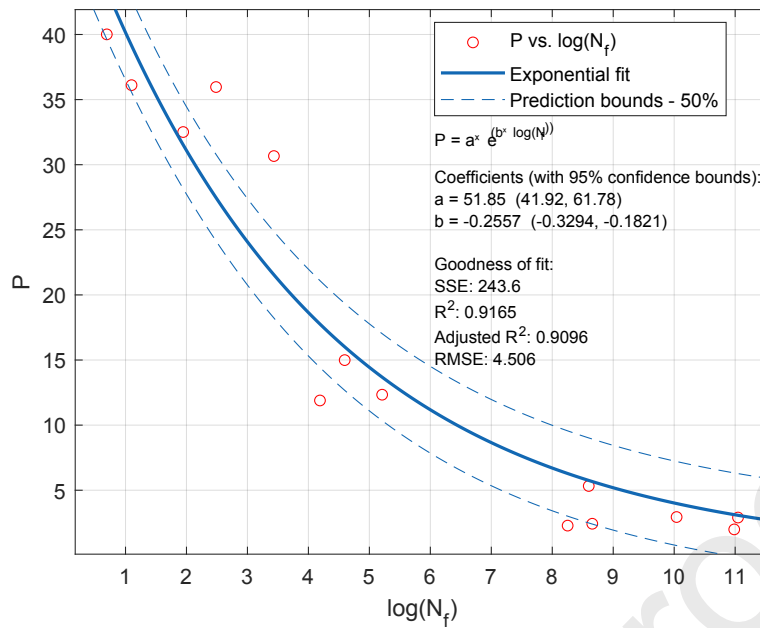
Fig. 19. Topographic stress factor *P* vs. number of cycles to failure for the tested cases.
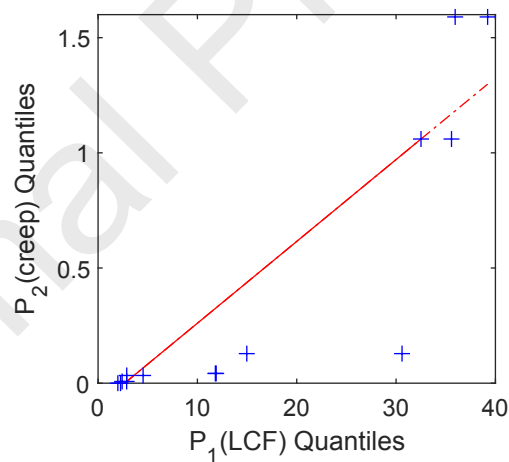

**Fig. 20.** Quantile-quantile plot quantifying the damage fraction of creep and LCF.

Fig. 20 displays a quantile-quantile plot created from both the P_1 quantity associated with the LCF loading ($\frac{Vv\,D_f}{Sq}\varepsilon_a\,\sigma_a$) and the P_2 quantity associated with the creep history ($\varepsilon_{creep}\,\sigma_{creep}$). A quantile-quantile plot orders the sample data values from smallest to largest, then plots these values against the expected value for the specified distribution at each quantile in the sample data. The plot shows that the damage fraction of creep (P_2) is smaller than the damage fraction of LCF (P_1). The plot is not a straight line, suggesting that the P_2 - P_1 data do not follow a normal distribution.

The number of cycles to failure in natural logarithmic coordinates log(N_f) and the fitted number of cycles to failure in natural logarithmic coordinates log(N_{fcal}) computed from the topographic stress factor P obtained from the experimental data (the exponential equation displayed in Fig. 19) is compared in Fig. 21. The experimental fatigue life N_f and the calculated fatigue life $N_{f\ cal}$ computed from the fracture surface parameter P (see Eq. (2)) is compared in Fig. 21(a). The results obtained with the proposed P parameter are also compared with those obtained by Tomczyk and Seweryn [21] or Falkowska et al.[43] (see Fig. 21(b)). This approach states that in a single fatigue load cycle, the increase of the damage parameter ω depends on the increase of plastic strain dε_p

$$\Delta\omega = \frac{A_\omega}{\sigma_c^{n_\omega}} \int_0^{\varepsilon_{ap}} \sigma^{n_\omega} d\varepsilon_p, \qquad (3)$$

where σ_c is the nominal critical stress, and A_ω and n_ω are material parameters.

As can be seen, both calculations correlate well with the experimental results for these cases of mixed loading conditions. Confidence and prediction bounds define the lower and upper values of the associated interval and define the width of the interval. The width of the interval indicates how uncertain are the fitted coefficients, the predicted observation, or the predicted fit. The bounds are defined with a level of certainty of 90%. It gives a 10% chance of being incorrect about predicting a new observation. This interval indicates 90% chance that the new fatigue test result is actually contained within the lower and upper prediction bounds.

(a) log($N_{f\ cal}$) vs. log(N_f)
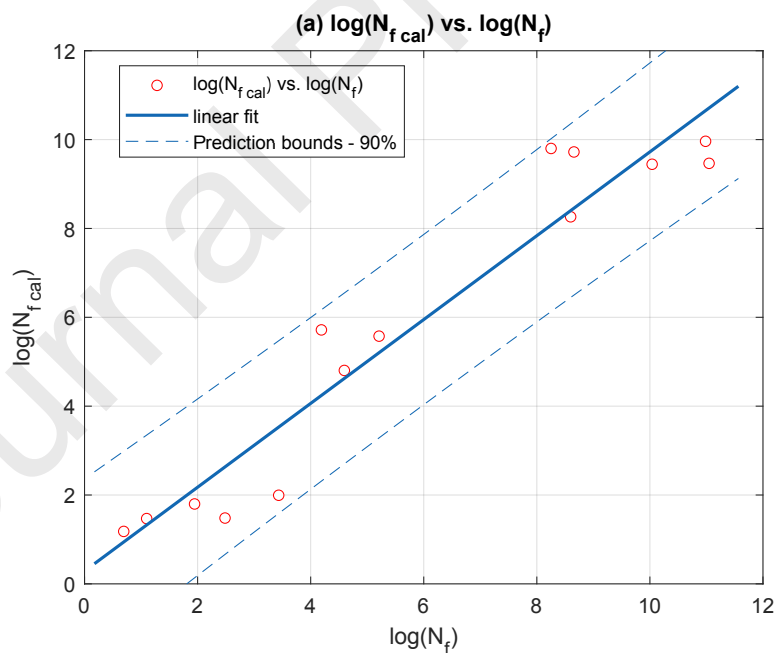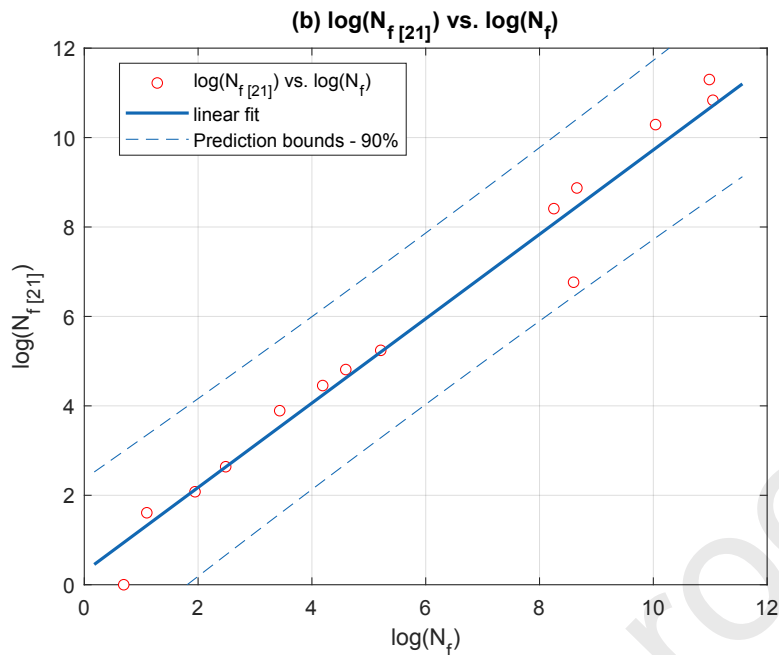
Fig. 21. The fitted number of cycles to failure in natural logarithmic coordinates: (a) $\log(N_{f\,cal})$ computed from the topographic stress factor P versus. the number of cycles to failure in natural logarithmic coordinates $\log(N_f)$; (b) predicted number of cycles to failure according to Tomczyk and Seweryn [21] in natural logarithmic coordinates $\log(N_f)$ versus. the number of cycles to failure in natural logarithmic coordinates $\log(N_f)$.

4. Summary and conclusions

The effect of the mixed creep and LCF fracture surface parameters has been studied for EN-AW 2024 aluminum alloy. A quantitative analysis with the entire fracture surface method of the tested specimens was performed for each loading case. A new topographic stress factor P based on the fracture surface state combined with the strain and stress amplitudes and also with the creep strain and creep strain is proposed to assess the durability. The conclusions can be summarized as follows:

- The creep history had a strong influence not only on fatigue life but also on surface topography measurements, either using area Sx, volume Vx or fractal dimension D_f parameters;

- The creep and LCF effects can be examined using Sx, Vx and D_f parameters but also have a strong influence on other such indicators, such as texture isotropy, furrows depth and slope isotropy;

- The values of maximum depth of furrows for LCF fractures are smaller for a creep temperature equal to 300°C than for 100°C;

- In the case of low values of ε_a, the damage initiation process begins on the external surface of the specimen with a clearly visible propagation stage;

- For large values of ε_a, the initiation takes place in the axis of the sample and is governed by the principal stress σ_I or the principal strain, ε_I.

- Formation of a fine-grained structure, as a result of recrystallization during creep at elevated temperature, significantly affects the improvement of fatigue life in the area dominated by plastic deformation and deterioration in the area dominated by elastic deformation;

- Significant mechanical hardening during creep at 100°C deteriorates fatigue life for high plastic deformation region;

- The new post-failure equivalent topographic stress factor P seems to reflect the physical failure conditions of this material under creep and LCF loads;

- The fatigue lives predicted using the proposed model agreed well with the experiments, with all points within prediction bounds 90%;

- The results obtained with the new model are within the same accuracy bounds (90%) as the Fakowska, Tomczyk and Seweryn's model, but the proposed approach is faster and simpler to implement, which can be advantageous.

Future research should focus on the broad data mining by utilizing other tested materials and loading scenarios via the introduction of data-driven approaches.

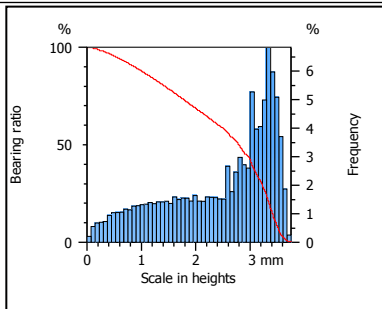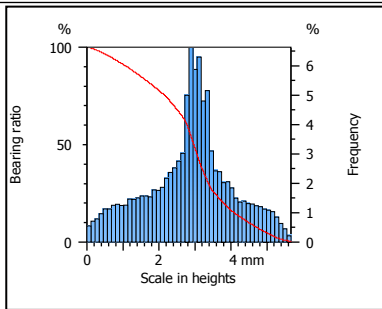## Acknowledgement

References

1. Tomczyk A, Seweryn A. Fatigue life of EN AW-2024 alloy accounting for creep pre-strain at elevated temperature. *Int J Fatigue* 2017; 103: 488–507.

2. Szala M, Chocyk D, Skic A, et al. Effect of Nitrogen Ion Implantation on the Cavitation Erosion Resistance and Cobalt-Based Solid Solution Phase Transformations of HIPed Stellite 6. *Materials 2021, Vol 14, Page 2324* 2021; 14: 2324.

3. Macek W, Pejkowski Ł, Branco R, et al. Fatigue fracture surface metrology of thin-walled tubular austenitic steel specimens after asynchronous loadings. *Eng Fail Anal* 2022; 138: 106354.

4. Branco R, Costa JD, Borrego LP, et al. Notch fatigue analysis and life assessment using an energy field intensity approach in 7050-T6 aluminium alloy under bending-torsion loading. *Int J Fatigue* 2022; 162: 106947.

5. Choi H, Lim HJ, Yun GJ. An integrated unified elasto-viscoplastic fatigue and creep damage model with characterization method for structural analysis of nickel-based high-temperature structure. *https://doi.org/101177/10567895221124324*. Epub ahead of print 13 September 2022.

6. Carpinteri A, Ronchei C, Spagnoli A, et al. On the use of the Prismatic Hull method in a critical plane-based multiaxial fatigue criterion. *Int J Fatigue* 2014; 68: 159–167.

7. Carpinteri A, Ronchei C, Spagnoli A, et al. Lifetime estimation in the low/medium-cycle regime using the Carpinteri–Spagnoli multiaxial fatigue criterion. *Theoretical and Applied Fracture Mechanics* 2014; 73: 120–127.

8. Macek W, Łagoda T, Mucha N. Energy-based fatigue failure characteristics of materials under random bending loading in elastic-plastic range. *Fatigue Fract Eng Mater Struct*. Epub ahead of print 2017. DOI: 10.1111/ffe.12677.

9. Branco R, Costa JD, Martins Ferreira JA, et al. Multiaxial fatigue behaviour of maraging steel produced by selective laser melting. *Mater Des* 2021; 201: 109469.
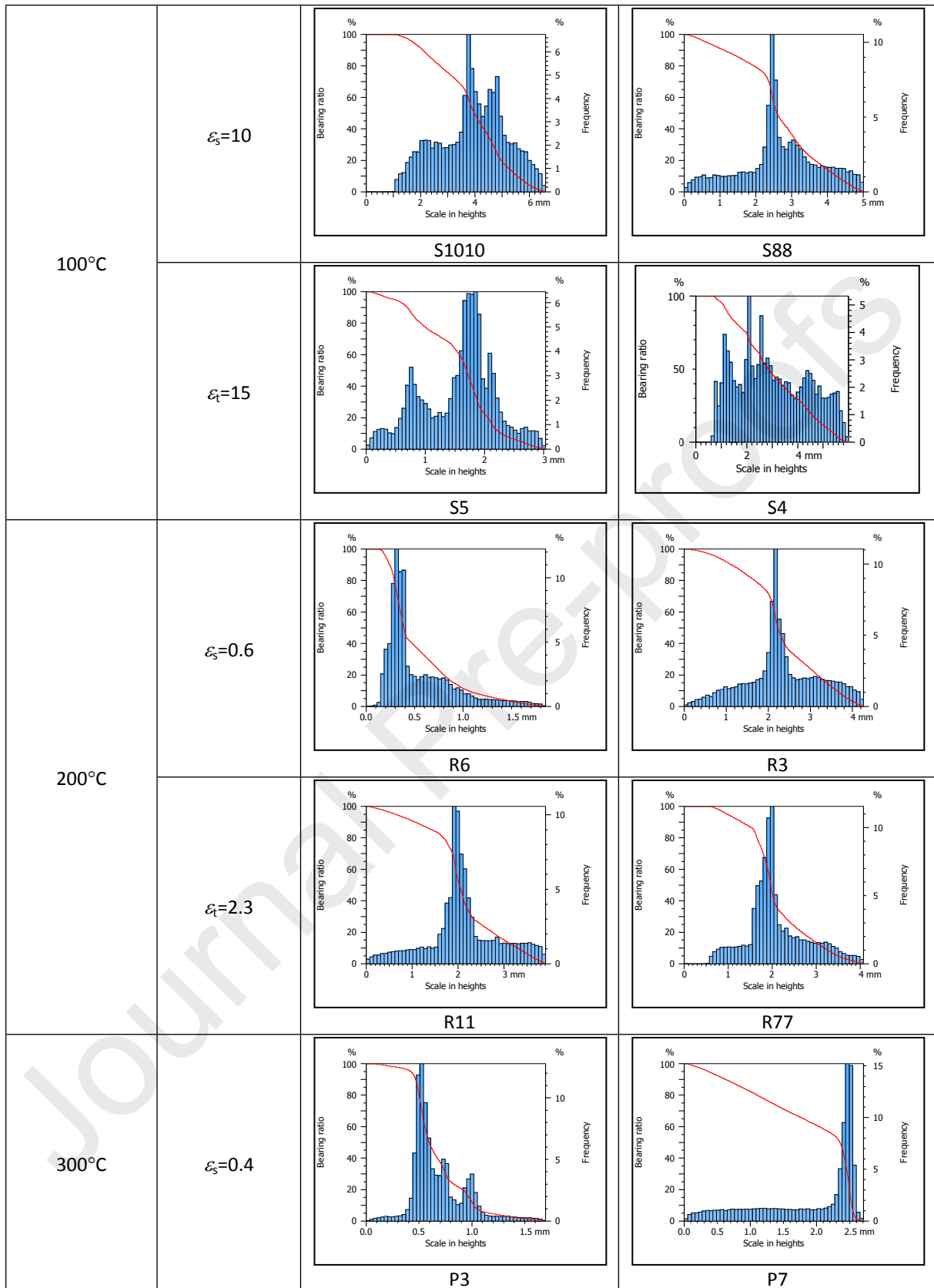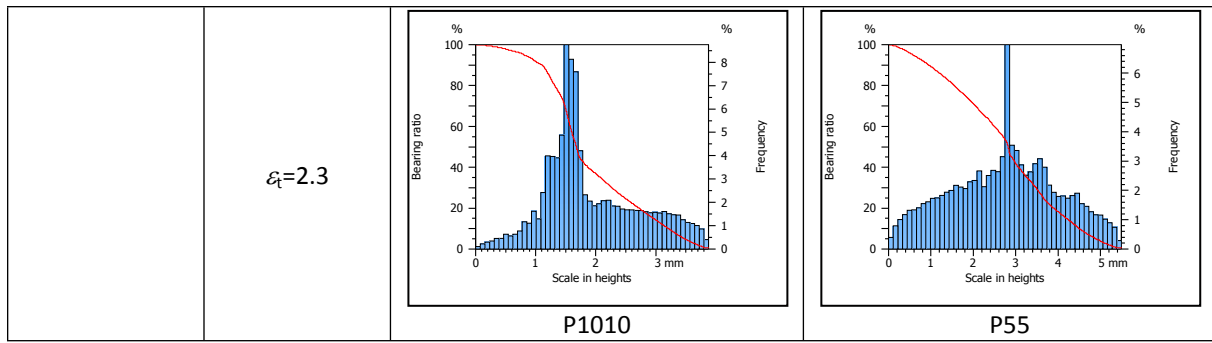
10. Rozumek D, Lewandowski J, Lesiuk G, et al. The energy approach to fatigue crack growth of S355 steel welded specimens subjected to bending. *Theoretical and Applied Fracture Mechanics* 2022; 121: 103470.

11. Vojtek T, Hohenwarter A, Pippan R, et al. Experimental evidence of a common local mode II growth mechanism of fatigue cracks loaded in modes II, III and II + III in niobium and titanium. *Int J Fatigue* 2016; 92: 470–477.

12. Pelegatti M, Lanzutti A, Salvati E, et al. Cyclic Plasticity and Low Cycle Fatigue of an AISI 316L Stainless Steel: Experimental Evaluation of Material Parameters for Durability Design. *Materials* 2021; 14: 3588.

13. Stamoulis G, Carrere N. Linear elastic analysis of the loading rate dependency of the fracture properties of structural adhesives in the mixed mode I+II plane. *Eng Fract Mech* 2020; 106840.

14. Deng QY, Zhu SP, Niu X, et al. Load path sensitivity and multiaxial fatigue life prediction of metals under non-proportional loadings. *Int J Fatigue* 2023; 166: 107281.

15. Zhu D, Zhang W, Ding Z. A modified fatigue damage model considering loading sequence effect. *https://doi.org/101177/10567895221088029* 2022; 31: 1027–1056.

16. Macek W, Owsiński R, Trembacz J, et al. Three-dimensional fractographic analysis of total fracture areas in 6082 aluminium alloy specimens under fatigue bending with controlled damage degree. *Mechanics of Materials*; 147. Epub ahead of print 1 August 2020. DOI: 10.1016/j.mechmat.2020.103410.

17. Masoudi Nejad R, Sina N, Ghahremani Moghadam D, et al. Artificial neural network based fatigue life assessment of friction stir welding AA2024-T351 aluminum alloy and multi-objective optimization of welding parameters. *Int J Fatigue* 2022; 160: 106840.

18. Sonntag N, Jürgens M, Skrotzki B, et al. Creep-fatigue of P92 in service-like tests with combined stress- and strain-controlled dwell times. *Int J Fatigue* 2023; 168: 107381.

19. Hormozi R, Biglari F, Nikbin K. Experimental and numerical creep–fatigue study of Type 316 stainless steel failure under high temperature LCF loading condition with different hold time. *Eng Fract Mech* 2015; 141: 19–43.

20. Sun L, Zhang XC, Wang RZ, et al. Evaluation of fatigue and creep-fatigue damage levels on the basis of engineering damage mechanics approach. *Int J Fatigue* 2023; 166: 107277.

21. Tomczyk A, Seweryn A. Experimental investigations and damage growth modeling of EN-AW 2024 aluminum alloy under LCF loading accounting creep pre-strain. *Fatigue Fract Eng Mater Struct* 2022; 45: 2703–2720.

22. Todhunter LD, Leach RK, Lawes SDA, et al. Industrial survey of ISO surface texture parameters. *CIRP J Manuf Sci Technol* 2017; 19: 84–92.

23. Santus C, Romanelli L, Grossi T, et al. Torsional-loaded notched specimen fatigue strength prediction based on mode I and mode III critical distances and fracture surface investigations with a 3D optical profilometer. *Int J Fatigue* 2022; 161: 106913.

24. International Organisation of Standardization. ISO 25178. *Geometric Product Specifications (GPS) – Surface texture: areal*.

25. Podulka P. Selection of Methods of Surface Texture Characterisation for Reduction of the Frequency-Based Errors in the Measurement and Data Analysis Processes. *Sensors 2022, Vol 22, Page 791* 2022; 22: 791.

26. Mandelbrot BB, Passoja DE, Paullay AJ. Fractal character of fracture surfaces of metals. *Nature* 1984; 308: 721–722.

27. Bouchaud E, Lapasset G, Planès J. Fractal Dimension of Fractured Surfaces: A Universal Value? *Europhys Lett* 1990; 13: 73.

28. Macek W, Robak G, Żak K, et al. Fracture surface topography investigation and fatigue life assessment of notched austenitic steel specimens. *Eng Fail Anal* 2022; 135: 106121.

29. EN ISO 204, 2009, Metallic materials, uniaxial creep testing in tension: method of test.

30. Manson SS. Behavior of materials under conditions of thermal stress. National Advisory Committee for Aeronautics. Report No. NACA TN-2933, 1954.

31. Coffin LF. A study of the effect of cyclic thermal stresses on a ductile metal. *Trans ASME*. 1954;76: 931–50.

32. Basquin OH. The exponential law of endurance tests. *ASTM Proc.* 1910;10: 625–30.

33. ISO 25178-2:2012 Geometrical Product Specifications (GPS) – Surface texture: Areal, Part 1: Terms, definitions and surface texture parameters.

34. Macek W. Post-failure fracture surface analysis of notched steel specimens after bending-torsion fatigue. *Eng Fail Anal* 2019; 105: 1154–1171.

35. Tomczyk A, Seweryn A. Experimental Investigation and Modeling of Damage Accumulation of EN-AW 2024 Aluminum Alloy under Creep Condition at Elevated Temperature. *Materials* 2021; 14: 404.

36. Macek W, Branco R, Costa JD, Trembacz J. Fracture Surface Behavior of 34CrNiMo6 High-Strength Steel Bars with Blind Holes under Bending-Torsion Fatigue, *Materials* 2022; 15: 80.

37. Sakai T, Belyakov A, Kaibyshev R, Miura H, Jonas JJ. Dynamic and post-dynamic recrystallization under hot, cold and severe plastic deformation conditions. *Prog Mater Sci*. 2014; 60: 130-207.

38. Tomczyk A, Seweryn A, Grądzka-Dahlke M. The effect of dynamic recrystallization on monotonic and cyclic behaviour of Al-Cu-Mg alloy. *Materials*. 2018; 11: 874.

39. Tomczyk A, Seweryn A, Doroszko M. Monotonic behaviour of typical Al-Cu-Mg alloy pre-strained at elevated temperature. *Journal of Theoretical and Applied Mechanics* 2018; 56: 1055-1068.

40. Glinka G. Energy density approach to calculation of inelastic strain-stress near notches and cracks. *Eng Fract Mech* 1985; 22: 485–508.

41. Macha E, Sonsino CM. Energy criteria of multiaxial fatigue failure. *Fatigue Fract Eng Mater Struct* 1999; 22: 1053–1070.

42. Branco R, Martins RF, Correia JAFO, et al. On the use of the cumulative strain energy density for fatigue life assessment in advanced high-strength steels. *Int J Fatigue* 2022; 164: 107121.

43. Falkowska A, Seweryn A, Szusta J. Predicting the fatigue strength and life of 316L steel sinters of varying porosity for implants in a uniaxial loading state. *Eng Fract Mech.* 2018; 200: 146–165.

Appendix A1. Histograms and Abbott curves for analyzed fractures

Pre-strain temperature	Pre-strain level (ε_s or ε_t) [%]	Lower loading amplitudes	Higher loading amplitudes
as-received			
		(1)	(2)

100°C	ε_s=10	 S1010	 S88
	ε_t=15	 S5	 S4
200°C	ε_s=0.6	 R6	 R3
	ε_t=2.3	 R11	 R77
300°C	ε_s=0.4	 P3	 P7

| | ε_t=2.3 | P1010 | P55 |

Fig. A1. Histograms and Abbott curves of fatigue fractures obtained for as-received material and for material with different history of creep pre-strain for lower and higher values of the load amplitude ε_a

Declaration of interests

☒ The authors declare that they have no known competing financial interests or personal relationships that could have appeared to influence the work reported in this paper.

☐ The authors declare the following financial interests/personal relationships which may be considered as potential competing interests:

- The effect of creep pre-strain on LCF failure is examined via fractographic analysis for 2024 AA
- S_x, V_x and D_f fracture surface parameters were strongly dependent on the creep pre-strain history
- A new damage parameter P combining fracture surface topography and load features is introduced
- The proposed damage parameter P can successfully estimate the fatigue lifetime for 2024 AA